The role of subtropical Rossby waves in amplifying the divergent circulation of the Madden Julian Oscillation

Pragallva Barpanda[1], Stefan Tulich[1], Juliana Dias[2], and George N Kiladis[2]

[1]CIRES
[2]NOAA, Physical Sciences Laboratory, Boulder, CO, USA

December 7, 2022

Abstract

The composite structure of the Madden-Julian Oscillation (MJO) has long been known to feature pronounced Rossby gyres in the subtropical upper troposphere, whose existence can be interpreted as the forced response to convective heating anomalies in the presence of a subtropical westerly jet. Here we inquire as to whether these forced gyre circulations have any subsequent effects on divergence patterns in the tropics. A nonlinear spherical shallow water model is used to investigate how the introduction of different background jet profiles affects the model's steady-state response to an imposed MJO-like thermal forcing. Results show that a stronger jet leads to a stronger Kelvin-mode response in the tropics up to a critical jet speed, along with stronger divergence anomalies in the vicinity of the forcing. To understand this behavior, additional calculations are performed in which a localized vorticity forcing is imposed in the extratropics, without any thermal forcing in the tropics. The response is once again seen to include pronounced equatorial Kelvin waves, provided the jet is of sufficient amplitude. A detailed analysis of the vorticity budget reveals that the zonal-mean zonal wind shear plays a key role in amplifying the Kelvin-mode divergent winds near the equator. These results help to explain why the MJO tends to be strongest during boreal winter when the Indo-Pacific jet is typically at its strongest.

Posted on 7 Dec 2022 — CC-BY 4.0 — https://doi.org/10.1002/essoar.10512829.1 — This a preprint and has not been peer reviewed. Data may be preliminary.

Generated using the official AMS LaTeX template v6.1

The role of subtropical Rossby waves in amplifying the divergent circulation of the Madden Julian Oscillation

Pragallva Barpanda,[1,2] Stefan Tulich,[1,2] Juliana Dias,[2] George N. Kiladis,[2]

[1] *CIRES, University of Colorado, Boulder, CO, USA*

[2] *NOAA, Physical Sciences Laboratory, Boulder, CO, USA*

Corresponding author: Pragallva Barpanda, pragallva.barpanda@noaa.gov

ABSTRACT: The composite structure of the Madden-Julian Oscillation (MJO) has long been known to feature pronounced Rossby gyres in the subtropical upper troposphere, whose existence can be interpreted as the forced response to convective heating anomalies in the presence of a subtropical westerly jet. Here we inquire as to whether these forced gyre circulations have any subsequent effects on divergence patterns in the tropics. A nonlinear spherical shallow water model is used to investigate how the introduction of different background jet profiles affects the model's steady-state response to an imposed MJO-like thermal forcing. Results show that a stronger jet leads to a stronger Kelvin-mode response in the tropics up to a critical jet speed, along with stronger divergence anomalies in the vicinity of the forcing. To understand this behavior, additional calculations are performed in which a localized vorticity forcing is imposed in the extratropics, without any thermal forcing in the tropics. The response is once again seen to include pronounced equatorial Kelvin waves, provided the jet is of sufficient amplitude. A detailed analysis of the vorticity budget reveals that the zonal-mean zonal wind shear plays a key role in amplifying the Kelvin-mode divergent winds near the equator. These results help to explain why the MJO tends to be strongest during boreal winter when the Indo-Pacific jet is typically at its strongest.

SIGNIFICANCE STATEMENT: The MJO is a planetary-scale convectively coupled equatorial disturbance that serves as a primary source of atmospheric variability on intraseasonal timescales (30-90 days). Due to its dominance and spontaneous recurrence, the MJO has a significant global impact, influencing hurricanes in the tropics, storm tracks and atmosphere blocking events in the midlatitudes, and even weather systems in the polar region. Despite steady improvements in S2S (subseasonal-to-seasonal) forecast models, the MJO prediction skill has still not reached its maximum potential. The root of this challenge is partly our deficient understanding of how the MJO interacts with the background mean flow. In this work we use a simple one layer atmospheric model with idealized heating to understand the impact of the subtropical jet on the MJO amplitude and its horizontal structure.

1. Introduction

The Madden-Julian Oscillation (MJO) is a planetary-scale equatorial disturbance that dominates tropical variability on the intraseasonal timescales. The disturbance is typified by a zonal dipole pattern in convective heating and cooling that moves eastward at a phase speed of $\sim$ 5m/s. The heating/cooling extends through the depth of the troposphere and drives horizontal divergence/convergence at upper levels ($\sim$ 200hPa) and convergence/divergence below (Kiladis et al. 2005, and references therein). The upper-tropospheric component of the MJO's circulation has a much larger meridional extent than its lower-tropospheric component and is marked by pronounced off-equatorial cyclonic and anticyclonic Rossby gyres whose centers lie in the subtropics (Knutson and Weickmann 1987; Rui and Wang 1990; Kiladis and Weickmann 1992; Hendon and Salby 1994; Kiladis et al. 2005).

The Rossby gyres are thought to be a result of interaction between the convectively forced divergent flow with the basic state vorticity gradient, known as the Rossby wave source (Sardeshmukh and Hoskins 1988). Wintertime MJO composites reveal that these gyres form on the southern flank of the subtropical westerlies, move eastward in-tandem with the MJO convection and are most pronounced in the Indo-Pacific sector – a region where both MJO convective activity and the subtropical jet are found to be the strongest in the boreal winter (Adames and Wallace 2014). The relative location of the MJO-induced Rossby gyres with respect to the climatological background flow affects extratropical teleconnection patterns that influence global weather on subseasonal-to-

seasonal timescales (Liebmann and Hartmann 1984; Weickmann et al. 1985; Lau and Lau 1986; Lau and Phillips 1986; Knutson and Weickmann 1987; Ferranti et al. 1990; Hoskins and Ambrizzi 1993; Jin and Hoskins 1995; Hsu 1996; Matthews et al. 2004; Lin et al. 2010; Seo and Lee 2017; Tseng et al. 2019; Hall et al. 2020). However, the connection between the MJO and extratropics is not just in one direction.

There have been several different studies indicating that variability in the extratropics potentially has an important influence on the MJO. Among the earliest is the study by Straus and Lindzen (2000) who documented a strong coherence between slow eastward-propagating circulation signals in the subtropical upper troposphere and MJO zonal winds in the tropics. Although they attributed the subtropical low-frequency variability to planetary-scale baroclinic instability (Frederiksen and Frederiksen 1997), the baroclinic generation of extratropical long-waves is not well-understood, and remains an active area of research (Hsieh et al. 2021; Moon et al. 2022). On the modelling side, Lin et al. (2007) used a dry atmospheric model with a winter-time basic state and showed that an MJO-like response (in the form of a slow planetary-scale Kelvin wave with 15 m/s phase speed) can be generated in the Eastern Hemisphere by an imposed subtropical forcing. Ray and Zhang (2010) also performed experiments using a tropical channel model and were able to initiate an MJO event by including extratropical influence via lateral boundary conditions. Subsequently, Ray and Li (2013) performed mechanism denial experiments and showed that they could eliminate the MJO by cutting off extratropical waves. A potential issue with that study, however, was later identified by Ma and Kuang (2016), who performed more carefully designed experiments showing that the MJO 'can exist without extratropical influence', provided the basic state is maintained. At the same time, there are some competing MJO theories based on the dynamics of Rossby vortices that implicitly include extratropical influences on the MJO (Yano and Tribbia 2017; Rostami and Zeitlin 2019; Hayashi and Itoh 2017).

Such disparate studies have led to some uncertainty about the mechanistic pathways through which extratropical circulations might affect the MJO. Nevertheless, there is broad agreement that the subtropical jet structure and attendant Rossby-gyres are important for providing a complete dynamical description of the MJO. While many studies have primarily focused on the forcing of subtropical circulations by the MJO (Schwendike et al. 2021, and references therein), here we focus

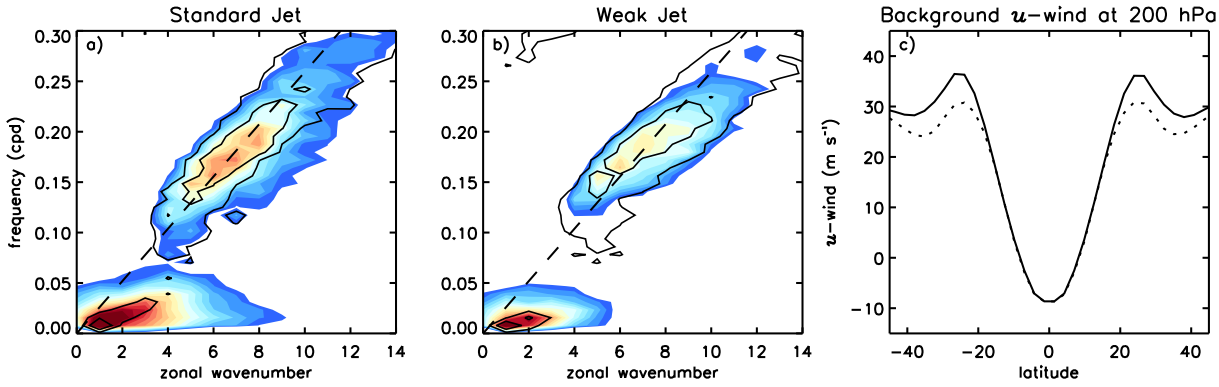

FIG. 1. Tropical rain spectra from Tulich and Kiladis (2021) for (a) standard IPAC and (b) weak IPAC jet experiments. (c) Comparison of zonal-mean zonal wind profiles at 200 hPa for standard IPAC (solid curve) and weak IPAC (dashed curve) cases. See their table 1 for experimental details.

on the opposite side of the coin, namely, how does the presence and strength of a subtropical jet affect the MJO?

Recently Tulich and Kiladis (2021), hereafter TK21 explored the impact of jet structure on the MJO and convectively-coupled Kelvin waves using aquaplanet experiments with the super-parameterized Weather Research and Forecast model (SP-WRF). Briefly, they prescribed zonally symmetric sea surface temperature and nudged the subtropics towards a desired wind profile. They found considerable weakening of the MJO signal when the zonal-mean Indo-Pacific (IPAC) subtropical jet was weakened by 25% (Fig. 1; see TK21 for details). Although the sophisticated SP-WRF modelling setup produced a reasonably realistic MJO, the model complexity masked the precise pathway by which the jet controlled the MJO strength.

To disentangle the feedback mechanism from the subtropics to the tropics, here we use a dry spherical shallow-water model with variable jet speeds and perform two type of forcing experiments, namely, MJO-like thermal forcing at the equator and MJO induced gyre-like vorticity forcing in the subtropics. We then use a steady-state vorticity budget to show how the Rossby-mode generated by each type of forcing experiments influences the Kelvin-mode divergence as a function of subtropical jet speed.

The paper is organized as follows. In section 2, we provide model details and outline the analytical approach for decomposing the model divergence into Matsuno-Gill modes and dynamical quantities

from the vorticity budget. Section 3 describes the results of the steady-state model response for different jet speeds in response to thermal forcing and vorticity forcing experiments. Finally, in section 4 we discuss and summarize our results.

2. Methods

a. Model setup

We use a nonlinear spherical shallow water model to investigate how the structure of the background flow affects the atmosphere's response to an imposed MJO-like forcing, in the absence of moisture effects[1]. The model setup is similar to that of Kraucunas and Hartmann (2007) and Monteiro et al. (2014). Briefly, the model solves for relative vorticity (ζ), divergence (D) and geopotential (ϕ) in spherical coordinates specified by latitude (θ) and longitude (λ). The complete set of equations is:

$$\frac{\partial \zeta}{\partial t} + \nabla.(\mathbf{v}\zeta_a) = F_\zeta - \frac{\zeta}{\tau_m} \quad (1)$$

$$\frac{\partial D}{\partial t} + \nabla \times (\mathbf{v}\zeta_a) - \nabla_H^2 (KE + \phi + \phi_T) = F_D - \frac{D}{\tau_m} \quad (2)$$

$$\frac{\partial \phi}{\partial t} + \nabla.(\mathbf{v}\phi) = F_\phi - \frac{(\phi - \phi_{eq})}{\tau_\phi} \quad (3)$$

where $\mathbf{v}$ is the horizontal wind vector (u, v), ζ_a is absolute vorticity given by $2\Omega\ sin\theta + \zeta$, Ω is the rotation rate of Earth, ∇ is the horizontal differential operator, KE denotes horizontal kinetic energy given by $\left(u^2 + v^2\right)/2$, and τ_m (τ_ϕ) is the momentum (geopotential) damping timescale. Here, F_ζ, F_D, and F_ϕ are generic forcing terms, where the geopotential forcing F_ϕ is analogous to thermal forcing in a stably stratified fluid. As conveyed by the last term in Eq. 3, the geopotential is relaxed to a fixed value $\phi_{eq} = gh_{\text{eq}}$, where h_{eq} is the fluid depth and g is the acceleration due to gravity. There is an additional "topographic" geopotential $\phi_T = gH_o cos^2\theta$ in Eq. 2, which is used to generate a background mean flow that conserves zonal-mean zonal angular momentum and whose strength is controlled by the parameter H_o. The default parameter settings are as follows unless otherwise stated: $F_D = 0$, $\tau_m = 20$ days, $\tau_\phi = 10$ days, $g = 9.8$ m/s ^{2}, $\Omega = 7.29 \times 10^{-5} s^{-1}$ and $h_{\text{eq}} = 500$ m. We also repeat our experiments for $h_{\text{eq}} = 200$ m.

[1]Original code is downloaded from https://nschaeff.bitbucket.io/shtns/shallow_water_8py-example.html and modified for the experiments.

The question of how the background flow structure affects the model's steady-state response to an imposed MJO-like forcing can be addressed in at least two different ways. The first (termed "Method 1") is to run the model through separate "spin-up" and "forcing" stages. During the spin-up stage, a stable subtropical jet is first generated by raising the zonally symmetric topography, i.e. H_o is increased from $0 \rightarrow H_{max}$. By day 50, the model reaches an equilibrium and H_{max} determines the maximum jet speed, U_{jet}. During the subsequent forcing stage, the MJO-like forcing is switched on and the model is run further to a steady-state equilibrium, which is typically reached in 200 days. While this technique has become standard in the literature (Kraucunas and Hartmann 2007; Bao and Hartmann 2014; Monteiro et al. 2014), it can be time consuming when considering a large number of different U_{jet} profiles.

A more efficient way of probing the effects of changes in U_{jet} (termed "Method 2") is to effectively combine the spin-up and forcing stages. Specifically, the model is initialized with a resting basic state ($H_o = 0$) and subjected to a steady MJO-like external forcing. Then over 600 days, U_{jet} is gradually increased by slowly raising the zonally symmetric topography, i.e. H_o is gradually increased from $0 \rightarrow 3500$ m allowing U_{jet} to span from 0 to 78 m/s, while being in quasi-equilibrium. The choice of 600 days is made to ensure that the contribution of jet acceleration to the momentum budget is negligibly small. In this way, the effects of altering U_{jet} can be assessed by simply treating each stage of the integration as a separate realization of the model's steady-state response to the forcing.

Throughout this paper, we mainly rely on Method 2 to examine how the model responds to an imposed MJO-like forcing under a wide range of U_{jet} values. A few runs are also considered using Method 1, to demonstrate that it yields similar results as Method 2.

1) Description of the background state

The specified background state is hemispherically symmetric with zero-mean winds at the equator, as an idealization of Earth's upper-tropospheric zonal-mean circulation. Figure 2a–c plot the model's steady-state zonal-mean horizontal winds $(\overline{U}, \overline{V})$ and geopotential $(\overline{\phi})$ for a range of different values of H_o. The zonal jet profiles in all cases satisfy a nonlinear balance relation (see Eq. (8) in Kraucunas and Hartmann 2007), which reduces to gradient wind balance in the zonal-mean for the tropics. As H_o is increased, the model's subtropical jet becomes stronger, which

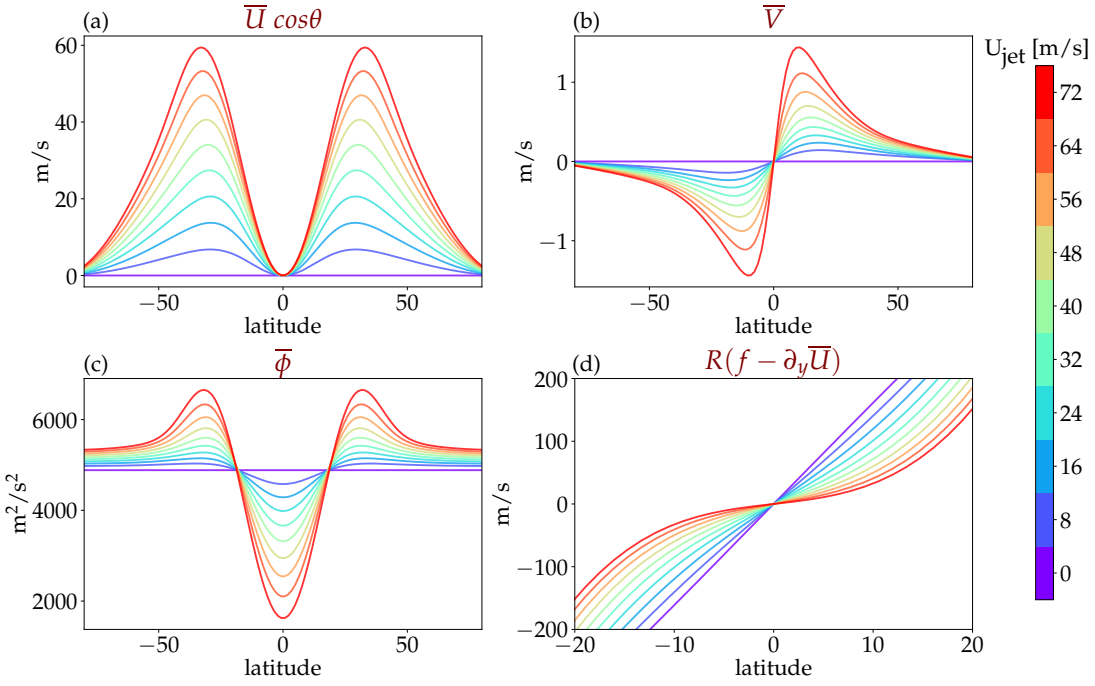

FIG. 2. Latitudinal profiles of the modeled background state (obtained using method 2; see text for details) in terms of the zonal-mean (a) zonal wind (b) meridional wind (c) geopotential, and (d) absolute vorticity in the tropics, color-coded for different values of U_{jet}. For convenience, zonal wind is scaled by cosine of latitude and absolute vorticity is scaled by the radius of Earth, R.

leads to stronger mean poleward flow representing upper-branch of the Hadley cell, along with a corresponding reduction of mean geopotential height in the tropics and buildup in the extratropics. As shown in Fig. 2d, these changes also lead to a reduction of the zonal-mean absolute vorticity gradient in the subtropics, which has an important bearing on the forcing of Rossby waves by divergent winds in the tropics (Sardeshmukh and Hoskins 1988). The increase in jet strength is also accompanied by a slight poleward shift in the jet maximum, as can be seen in Fig. 2a. Based on the results of additional calculations (not shown), we conclude that the effects of this shift are neglible in comparison to the effects of the changes in jet strength.

2) External forcing

The observed diabatic structure of the MJO typically consists of a dipole pattern of deep-tropospheric heating and cooling that moves eastward at a phase speed, $c_{\text{f}} \sim 5$ m/s (**?**). The

vertical profiles of the heating and cooling tend to be the largest in the mid to upper troposphere ($\sim$ 300 hPa), and thus project strongly onto vertical modes with equivalent depths in the range, $h_{\text{eq}} \sim 200\text{m} - 500\text{m}$ or gravity-wave speeds in the range, $c \sim 44 - 70$ m/s. The ratio of MJO phase speed to gravity wave speed is therefore generally close to 0, i.e. $c_{\text{f}}/c \sim 0$.

To mimic these observations, we perform a series of thermal forcing calculations where the forcing is applied as a heating dipole (F_ϕ) centered at the equator, with the remaining forcing terms $\left(F_\zeta, F_D\right)$ set to 0. The heating dipole is prescribed as

$$F_\phi = \frac{gQ_o}{\tau_Q} e^{-\left((\theta-\theta_o)^2/L_y^2\right)} F_\lambda, \tag{4}$$

$$\text{where } F_\lambda = \begin{cases} sin\left(k\left(\lambda-\lambda_o\right)\right) & \text{for } |\left(\lambda-\lambda_o\right)| \leq 2\pi/k \\ 0 & \text{for } |\left(\lambda-\lambda_o\right)| > 2\pi/k \end{cases}.$$

Here, Q_o is amplitude, L_y sets the meridional scale of the forcing and k is zonal wave number. The default parameters are: $Q_o = 10$ m, $L_y = 10^\circ$, $k = 2$. The heating location is stationary and is centered at $\theta_o = 0$N and $\lambda_o = 100$E. The value of Q_o is chosen such that the model evolution remains approximately linear, in that the nonlinear eddy terms ($\overline{\zeta' v'}$, $\overline{\zeta'\zeta'}$ etc.) remain negligibly small.

As discussed later in Section 3, results of the above thermal forcing experiments point to the fact that model's tropical divergence is strongly affected by Rossby waves excited in the subtropics. To isolate the impact of such Rossby waves, we perform an additional vorticity forcing experiment, where the forcing F_ζ takes the form of a dipole pattern in the extratropics, with the thermal and divergent forcings both set to 0. The vorticity forcing is prescribed as

$$F_\zeta = \frac{\nabla \times \mathbf{v}_\psi}{\tau_m} \left(e^{-(\theta-40^\circ)^2} + e^{-(\theta+40^\circ)^2}\right) \tag{5}$$

where $\mathbf{v}_\psi$ denotes the steady-state rotational winds obtained from one of the stationary thermal forcing runs, namely that with $U_{\text{jet}} = 40$ m/s, $h_{\text{eq}} = 500$ m and rest of the parameters having their default values. Here the rotational flow ($\mathbf{v}_\psi$) is calculated using Helmholtz decomposition (Arfken and Weber 2005).

b. Analytical approach

1) Modal decomposition

The MJO's horizontal circulation can be conceptually viewed as a superposition of the Matsuno-Gill steady-state Kelvin and Rossby waves (Gill 1980; Chao 1987; Wang and Rui 1990; Maloney and Hartmann 1998). To cast the model output in these terms, we perform a meridional mode decomposition using Parabolic Cylinder Functions (PCFs). The approach is similar to that of Yang et al. (2003), which enables separation of the model's steady-state response into contributions by: 1) the Kelvin mode, 2) the lowest-order Rossby mode, and 3) the remaining (symmetric) higher-order Matsuno modes. Stated mathematically:

$$\begin{pmatrix} u^* \\ v^* \\ \phi* \end{pmatrix} = \underbrace{\begin{pmatrix} u_K \\ v_K \\ \phi_K \end{pmatrix}}_{\text{Kelvin}} + \underbrace{\begin{pmatrix} u_R \\ v_R \\ \phi_R \end{pmatrix}}_{\text{Rossby}} + \underbrace{\begin{pmatrix} u_{HO} \\ v_{HO} \\ \phi_{HO} \end{pmatrix}}_{\text{Higher-order}} \tag{6}$$

where asterisks denote deviations about the zonal-mean, i.e. ($u^* = u - \overline{U}$). The Kelvin (K), Rossby (R) and higher order Matsuno modes are calculated using Eqs A5, A6 and A7 respectively (see appendix A). In a resting basic state ($U_{\text{jet}} = 0$), these modes correspond to the orthogonal eigenvectors of the linearized shallow water system on an equatorial beta-plane (Matsuno 1966; Gill 1980). In a non-resting basic state ($U_{\text{jet}} > 0$), the modes still form a complete orthonormal basis, but are only approximations of the actual eigenvectors, whose structures are somewhat modified due to the effects of the background flow (Zhang and Webster 1992). From Eq. (6), the horizontal eddy divergence can be decomposed as

$$\nabla.\mathbf{v}^* = \nabla.\mathbf{v}_K + \nabla.\mathbf{v}_R + \nabla.\mathbf{v}_{HO} \tag{7}$$

where $\mathbf{v}^*$ denotes horizontal eddy wind vector (u^*, v^*), $\mathbf{v}_K$ denotes (u_K, v_K), $\mathbf{v}_R$ denotes (u_R, v_R) and $\mathbf{v}_{HO}$ denotes (u_{HO}, v_{HO}). Note that Kelvin-mode meridional wind, $v_K = 0$.

2) Vorticity budget decomposition

In addition to the above modal decomposition, we diagnose the model eddy divergence from the steady-state vorticity balance equation (see Eq. (1)), which can be expressed as $\nabla.(\mathbf{v}\zeta_a) \approx F_\zeta$, assuming damping is weak. Linearizing this balanced relation about a zonally symmetric background state $(\overline{U}, \overline{V})$ and neglecting the nonlinear terms, the steady-state eddy divergence can then be decomposed as

$$\nabla.\mathbf{v}^* \approx \underbrace{\frac{-v^*\beta_{\text{eff}}}{\overline{\zeta}_a}}_{\text{Sverdrup effect}} + \underbrace{\frac{-\partial_y(\overline{V}\zeta^*)}{\overline{\zeta}_a}}_{\text{Hadley cell effect}} + \underbrace{\frac{-\overline{U}\partial_x\zeta^*}{\overline{\zeta}_a}}_{\text{Jet advection}} + \underbrace{\frac{F^*_\zeta}{\overline{\zeta}_a}}_{\text{Vorticity forcing}} \tag{8}$$

where ζ^* is relative eddy vorticity and $\beta_{\text{eff}} = \beta - \partial^2_{yy}\overline{U}$. The horizontal derivatives in Cartesian coordinates are $\partial_x = \frac{1}{R}\frac{\partial}{\partial\lambda}(\,.\,)$ and $\partial_y = \frac{1}{Rcos\,\theta}\frac{\partial}{\partial\theta}((\,.\,)cos\,\theta)$. Each term on the right-hand-side (RHS) of Eq. (8) is given a name that alludes to the dynamical process embodied by the numerator of that term. For example, the first term is referred to as the 'Sverdrup effect' (Gill 1980; Monteiro et al. 2014), since it represents the portion of divergence that can be attributed to anomalous meridional advection of the background absolute vorticity. The second term is referred to as the 'Hadley cell effect', since it represents the portion that can be attributed to meridional deposition of the eddy vorticity flux by the mean-meridional winds. Likewise, the third term is referred to as the 'jet advection', since it represents the zonal-advection of eddy vorticity by the zonal-mean zonal winds. And finally, the fourth term is the 'Vorticity forcing' which represents the contribution to divergence from external sources, which in the real world may involve nonlinear eddy-eddy interaction. In the thermal forcing experiments, F^*_ζ is set to zero.

Note that in Eq. (8) the denominator, $\overline{\zeta}_a$ goes to zero near the equator (see Fig. 2d), but not all the numerators tend to zero at the same rate leading to an issue of division by zero, especially in the Hadley cell term for very high jet speeds. For presentation purpose and to avoid infinities, we smooth each of the RHS terms in Eq. (8) using a convolution function in python language. The results presented in this paper are independent of the smoothing function.

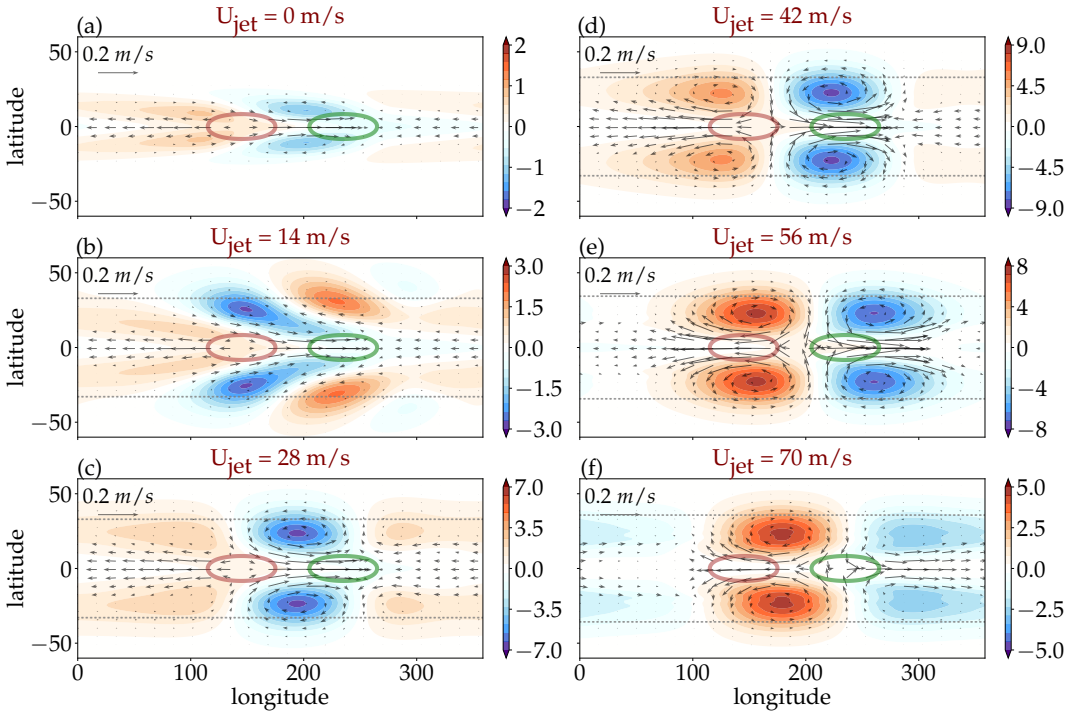

FIG. 3. Steady-state response to fixed MJO-like thermal forcing in terms of the eddy geopotential, ϕ^* in colors $[m^2/s^2]$ and eddy wind vectors, $\mathbf{v}^*$ [m/s] for background jet speeds U_{jet} of 0, 14, 28, 42, 56 and 70 m/s (panels a through f, respectively). Positive and negative thermal forcing regions are shown in brown and green contours respectively, which represent 1/4 of the maximum forcing. The dotted lines show the location of the jet maxima.

3. Results

a. Steady-state response to thermal forcing and variable jet speed

We first focus on the impact of the subtropical jet on the MJO's thermally forced circulation in the upper troposphere with fluid depth h_{eq} set at 500 m and U_{jet} ranging from 0 to 78 m/s. Setting h_{eq} = 500 m ensures that the mean fluid depth in the tropics is somewhere between 200 to 500 m, with the precise value depending inversely on the strength of the jet (see Fig. 2c).

1) SUBTROPICAL RESPONSE

Figure 3 shows the steady-state geopotential and wind anomalies excited by the stationary MJO-like thermal forcing for different subtropical jet speeds. The steady-state circulation obtained from Method 2 is comparable to Method 1 (see Fig. B1). In the familiar case where $U_{\text{jet}} = 0$ (Fig. 3a),

the positive part of the forcing induces a classic Gill-like pattern, consisting of a stationary Kelvin wave to the east and equatorial Rossby wave to the west of the mass-source or heating region (Gill 1980). This same Rossby-Kelvin pattern is also excited by the mass-sink or cooling region, but with opposite sign. As the jet speed increases, the equatorial Rossby wave response amplifies and shifts poleward, while the overall stationary wave pattern becomes meridionally tilted (shown for U_{jet} = 14 m/s in Fig. 3b). For even stronger jets, i.e. $U_{\text{jet}} \geq 28$ m/s, the equatorial Rossby waves transform into prominent subtropical gyres that are advected eastward with respect to the forcing (Figs. 3c-3f).

This systematic shift from an equatorial wave guide to a wider subtropical stationary wave pattern due to imposed changes in background jet strength was first reported by Monteiro et al. (2014), using a similar shallow water model setup. In addition to those authors' findings, we observe an interesting threshold behavior in the response that has not been previously documented. Specifically, for $U_{\text{jet}} \approx 0$ to $42m/s$, the overall strength of the subtropical gyres is seen to increase monotonically, while the opposite is seen for $U_{\text{jet}} \approx 42$ to $70m/s$.

An important difference between the model used here versus that of Monteiro et al. (2014) is in terms of the formulation of the geopotential tendency equation. Specifically, while those authors assumed a linear flux of the geopotential, by using a global mean equivalent depth in the geopotential equation (see Eq. (3) in their supplementary material), here we include the full nonlinear flux of the geopotential, i.e., $\nabla.(\phi\mathbf{v})$. As shown later, this difference has important implications for the divergent part of the eddy response in the tropics, whose dependence on jet speed is documented below.

2) Tropical response

Figure 4 shows the divergent part of the steady-state circulation for different values of U_{jet} where the divergent flow ($\mathbf{v}_\chi$) is determined using Helmholtz decomposition. The picture is broadly consistent with expectations, where net outflow from the heating region is balanced by net inflow to the cooling region. As the jet speed increases, the off-equatorial divergence and convergence anomalies associated with the subtropical cyclonic and anticyclonic vortices become more prominent on the poleward flanks of the forcing region. In the case of very strong jet speeds ($U_{\text{jet}} \geq$ 42m/s), the meridional component of the divergent winds become increasingly dominant

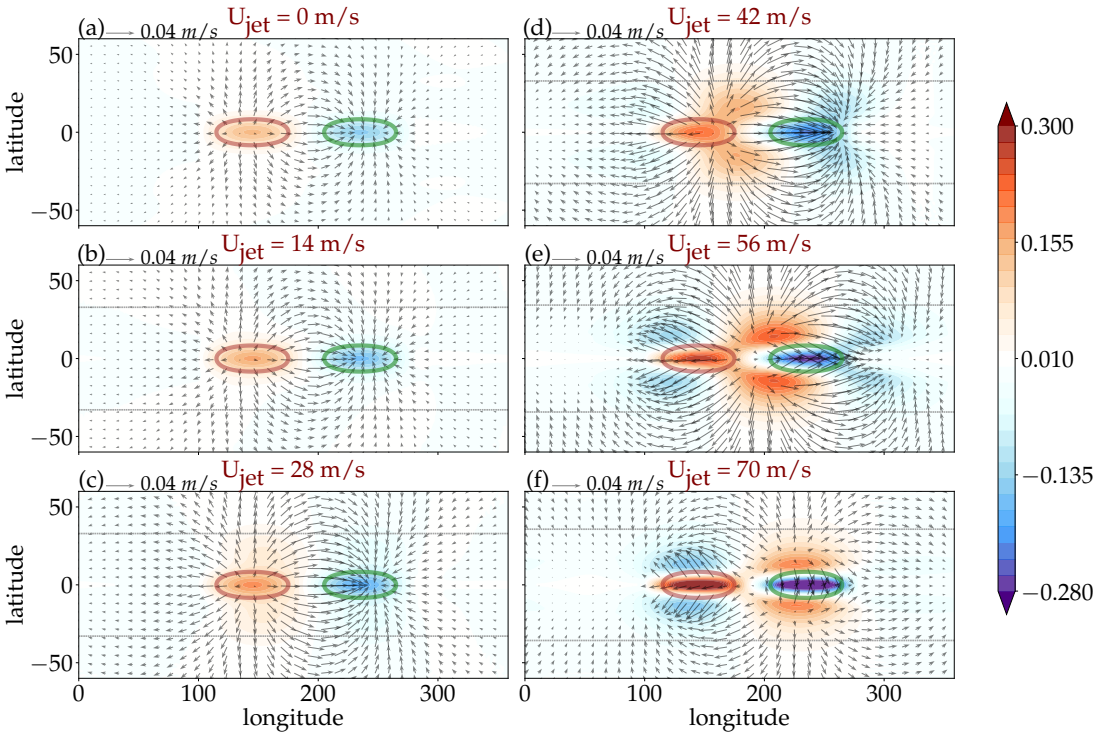

FIG. 4. Steady-state response to fixed MJO-like thermal forcing in terms of eddy divergence, $R\nabla.\mathbf{v}^*$ in colors [m/s] and divergent eddy wind vectors, $\mathbf{v}^*_\chi$ [m/s] for background jet speeds, U_{jet} set as 0, 14, 28, 42, 56 and 70 m/s (panels a through f, respectively). Positive and negative thermal forcing regions are shown in brown and green contours respectively, which represent 1/4 of the maximum forcing. The dotted lines show the location of the jet maxima. Divergence is rescaled by the radius of earth R for convenience.

.

over the zonal component, implying a transition in the dominant type of waves elicited by the forcing. Interestingly, the increasing U_{jet} also leads to an increase in the magnitude of eddy divergence at the forcing region. To leading order, the relation between eddy divergence and the jet speed near the forcing region can be understood by considering the following steady-state approximation of the linearized geopotential equation, Eq. (3) ,

$$\langle\overline{\phi}\rangle D^* \approx F^*_\phi \tag{9}$$

where $\langle\overline{\phi}\rangle$ is the zonal-mean tropical geopotential, $D^* = \langle\nabla.\mathbf{v}^*\rangle$ and angle brackets denote averaging between 10S −10N. The remaining linear terms, namely, $\overline{U}\partial_x\phi^*$, $\overline{V}\partial_y\phi^*$, $\phi^*\partial_y\overline{V}$, and $v^*\partial_y\overline{\phi}$ are

dropped from Eq. (9), since they are found to be of second-order importance when averaged between 10S-10N. By gradient wind balance, we know that $\langle\overline{\phi}\rangle$ decreases with increasing jet speed (See Fig. 2c), meaning eddy divergence (convergence) must increase in the heating (cooling) region to balance the fixed thermal forcing.

It is worth mentioning here that Eq. (9) is a statement of the weak-temperature gradient (WTG) approximation for a shallow water system (see Eq. 4 in Sobel et al. 2001). Therefore, we define the quantity, $\widetilde{D^*} \equiv F^*_\phi/\langle\overline{\phi}\rangle$, as the WTG divergence and use it as a baseline for interpreting changes in the actual divergence D^*. In a vertically stratified system, the equivalent geopotential, $\langle\overline{\phi}\rangle$ can be interpreted as the ratio of tropical static stability (Γ) to the vertical scale of the convective heating (L_z), i.e. $\langle\overline{\phi}\rangle = \Gamma/L_z$ (see Eq. 14 in Kiladis et al. 2009). This implies, the WTG divergence associated with MJO is linked to all three factors, namely, upper-level adiabatic heating/cooling, tropical static-stability and the vertical heating profile, all of which could be modified by the subtropical jet.

Globally, since the imposed net mass source is zero, the area-averaged eddy divergence must also be zero. However, at the forcing region the eddy divergence shows a jet speed dependence even with a fixed heat source. In order to capture the local amplification of divergence anomalies in the tropics, Fig. 5a shows the root-mean-square of eddy divergence averaged within the latitude band 10S to 10N (D^*_{RMS}; given by the cyan curve in Fig. 5a). To leading order, the increase of D^*_{RMS} with increasing jet speed broadly matches with the expectation from WTG approximation ($\widetilde{D^*}_{RMS}$; given by the orange dashed curve in Fig. 5a). However, the agreement is by no means perfect. The deviation between the actual divergence and WTG approximation ($\delta = D^*_{RMS} - \widetilde{D^*}_{RMS}$) grows with the increase in jet speed, reaches a maximum, then eventually decreases and becomes negative (given by the purple curve in Fig. 5a). This discrepancy is remarkable and confirms that the jet-speed dependence of the model's tropical divergence involves more than just the effect of changing $\langle\overline{\phi}\rangle$ as a consequence of gradient wind balance. The changes in δ_{RMS} primarily comes from the $v^*\partial_y\overline{\phi}$ term neglected in Eq. (9) (not shown), implying an important role for the underlying wave-mean flow interaction. To emphasize the threshold behavior of the divergent response, we define a critical jet speed, $U_c = 46$m/s at which δ_{RMS} reaches its peak value (given by black vertical line in Fig. 5a). The precise value of U_c, however, depends on the specified fluid depth, h_{eq} and phase speed of the thermal forcing (see Fig. C1 in Appendix C).

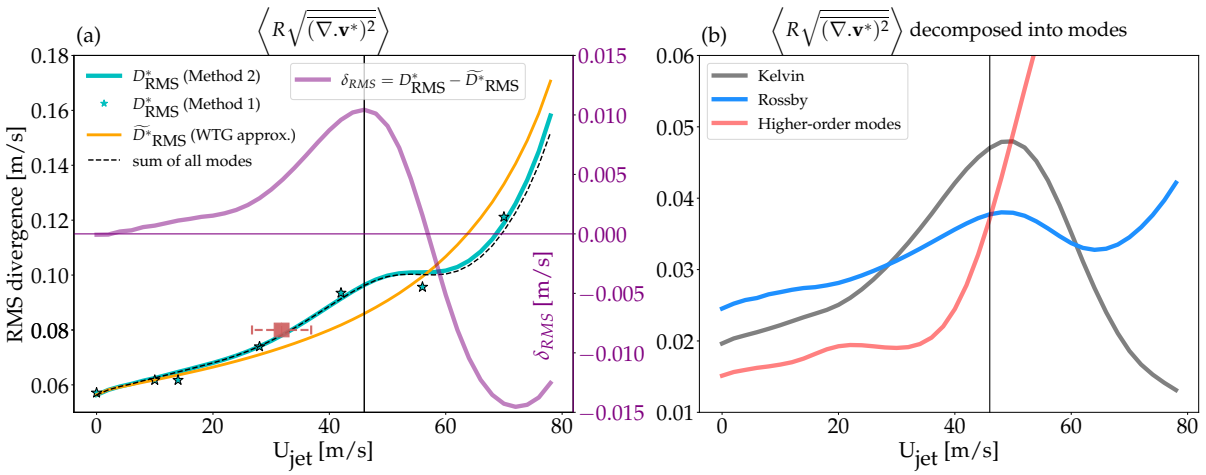

FIG. 5. Jet-speed dependence of (a) RMS eddy divergence in the tropics obtained from the model run (D^*_{RMS}; left y-axis), the WTG approximation ($\widetilde{D^*}_{\mathrm{RMS}}$; left y-axis) and the difference between the two (δ_{RMS}; right y-axis) and (b) D^*_{RMS} decomposed into Kelvin, Rossby and higher-order Matsuno modes (See Eq. (7)). In the left panel, the red boxplot marks the interannual variability of subtropical jet speed during winter-time (1979-2019) from ERA5, the stars and the solid cyan curve denote results from running steady state experiments using method 1 and 2 respectively and the black dashed curve is the linear sum of all the modes from Eq. (7). The black vertical line indicates an estimated critical jet speed, U_c (see text for details). The RMS divergence is calculated for the latitude band 10S −10N and then rescaled by the radius of Earth, R.

To give a ballpark for U_c, Earth's strongest subtropical jet occurs over the IPAC region during winter (Dec-Feb) and is $\sim 36 \pm 5$ m/s at 200 hPa when averaged over 20N - 55N latitude and 30E - 180E longitude. Within the range of interannual variability, Earth's current climate is within the limits of the critical jet speed (U_c) (as shown by the red boxplot in Fig. 5a).

To break down the response of D^*_{RMS} further, Fig. 5b shows how changes in U_{jet} affect the RMS eddy divergence for the Kelvin mode, lowest-order Rossby mode, and higher-order Matsuno modes (see Eqs. (6) and (7) for modal decomposition). As U_{jet} is increased, the Kelvin-mode amplitude (given by the grey curve in Fig. 5b) increases gradually before reaching its peak value at roughly the critical jet speed U_c and then decreases sharply thereafter. This behavior is different from that of the Rossby mode, whose amplitude (given by the blue curve in Fig. 5b) exhibits only modest deviations about an overall gradual increase across the entire span of U_{jet} values. The amplitude of the higher-order Matsuno modes (given by the red curve in Fig. 5b) remains relatively small for

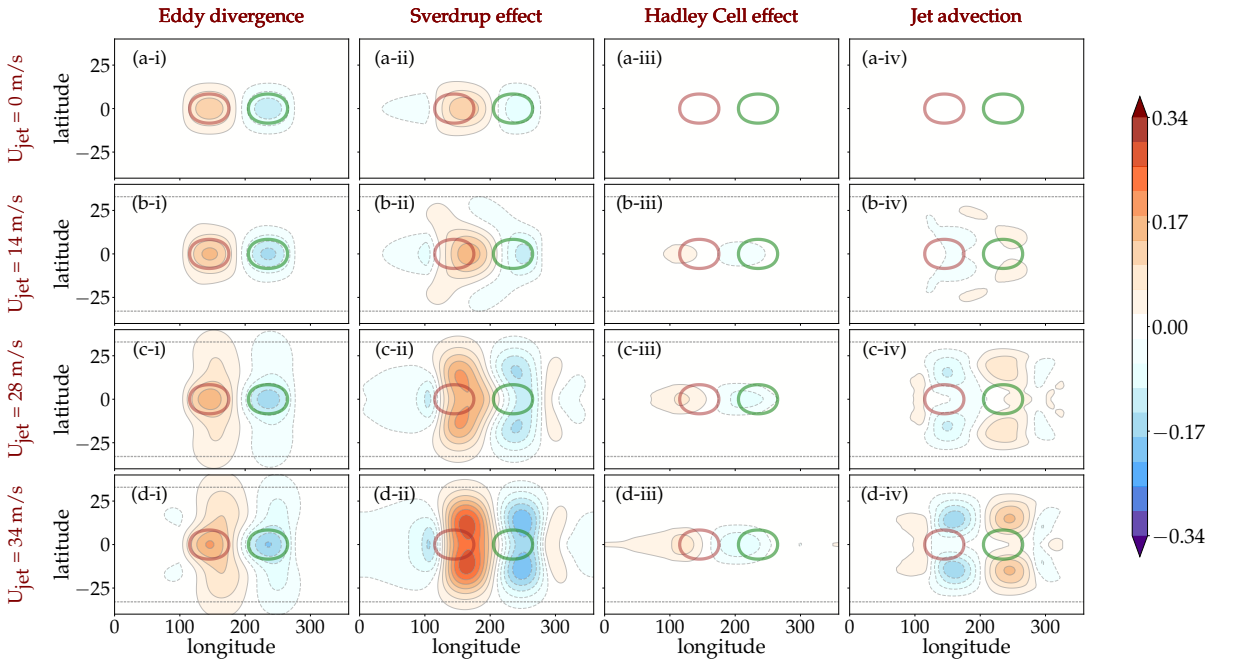

FIG. 6. Divergence budget for the weak jet regime ($U_{jet} < U_c$) as defined in Eq. (8) where (i) total eddy divergence is decomposed into contribution from (ii) Sverdrup effect, (iii) Hadley cell effect and (iv) jet advection where U_{jet} is set as 0, 14, 28 and 34 m/s (rows a through d, respectively) Divergence is rescaled by the radius of earth, R and is shown in units of m/s (colors). Positive and negative thermal forcing regions are shown in brown and green contours where contours represent 1/4 of the maximum forcing. The dotted line shows the location of the jet maxima.

jet speeds below $\sim$ 35 m/s, but increases sharply thereafter and eventually becomes dominant for $U_{\text{jet}} > U_c$.

To summarize, the jet-speed dependence of the model's divergence response to an imposed MJO-like thermal forcing exhibits two distinct regimes: (i) a "weak-jet" regime ($U_{\text{jet}} < U_c$) where the deviation between actual divergence and WTG divergence near the forcing region (δ_{RMS}) grows with the increase in jet speed mainly due to stronger amplification of Kelvin-divergence and (ii) a "strong-jet" regime ($U_{\text{jet}} > U_c$) where the deviation (δ_{RMS}) is reduced and becomes negative with increasing jet speed mainly due to a reduction in Kelvin-divergence, despite the increased contribution by the higher-order Matsuno modes.

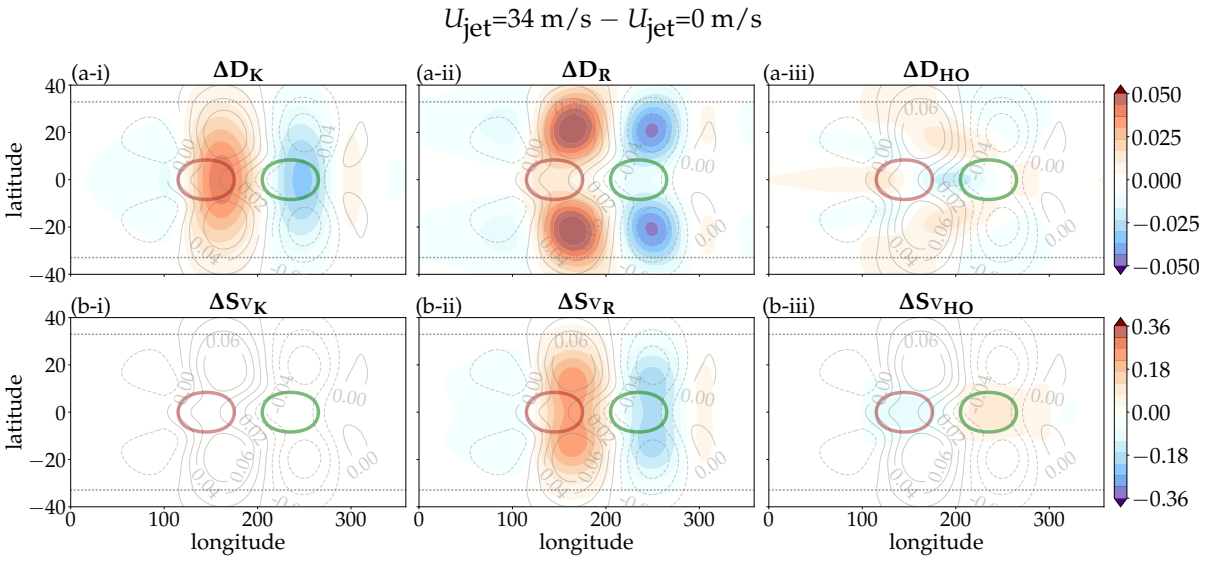

FIG. 7. Change in (a) eddy divergence and (b) Sverdrup effect between subtropical jet-state (U_{jet}=34 m/s) and resting basic-state (U_{jet}=0 m/s) experiments. Each row, (a) and (b) is decomposed into contribution from (i) Kelvin, (ii) Rossby and (iii) higher-order Matsuno modes as defined in Eq. (11). Gray solid (dashed) contours denote increase (decrease) in total divergence and is given by the sum of (a-i), (a-ii), (a-iii). Divergence is rescaled by the radius of earth, R and is shown in units of m/s (colors). Positive and negative thermal forcing regions are shown in brown and green contours where contours represent 1/4 of the maximum forcing.

3) WEAK JET REGIME

To identify the key dynamical processes behind the jet-speed dependence of the model's divergence response, we decompose eddy divergence from the steady-state vorticity budget to reflect contributions from the Sverdrup effect, the Hadley cell effect, and jet advection (see Eq. (8)). Figure 6 shows the divergence decomposition for the weak jet cases using Eq. (8). As expected from the steady-state mass-balance, eddy divergence at the forcing region is positive over the heat source and negative over the heat sink (see Fig. 6 a-i to d-i). In the absence of a jet, the local eddy divergence at the forcing region is primarily balanced by the Sverdrup effect (see Fig. 6 a-i) and has no contribution from the Hadley cell effect or jet advection. As the jet speed strengthens, the Sverdrup effect also strengthens and amplifies the local eddy divergence (see Fig. 6 a-ii to d-ii), particularly in the eastern flank of the forcing region due to zonally advected subtropical gyres (Fig. 3). With the strengthening jet, Hadley cell effect also becomes stronger, although its effect

is much weaker relative to the Sverdrup effect (see Fig. 6 a-iii to d-iii). For all cases, zonal wind advection has almost negligible role on the local divergence, rather its effect is only strong outside of the forcing region off the equator (see Figs. 6 a-iv to d-iv).

The important role of Sverdrup effect in the weak-jet regime suggests that any change in divergence at the forcing region is dynamically controlled by off-equatorial interaction between subtropical eddy (v^*) and the zonal-wind meridional shear ($\partial_y \overline{U}$) which is expressed as

$$\Delta\left(\nabla.\mathbf{v}^*\right) \approx \Delta\left(\frac{-v^*\beta_{\text{eff}}}{f-\partial_y\overline{U}}\right) \tag{10}$$

where Δ denotes change between two equilibrium states with different jet speeds. When the jet is stronger, both $(f-\partial_y\overline{U})$ and β_{eff} become smaller at the same rate, which means the ratio $\frac{\beta_{\text{eff}}}{f-\partial_y\overline{U}}$ tends to be constant for stronger and stronger jet speeds (not shown). Thus Eq. (10) implies that the increase/decrease of eddy divergence must be determined by the amplitude of meridional eddy winds ($|v^*|$) which predominantly comes from a strengthening Rossby wave source in the presence of stronger subtropical jet (Sardeshmukh and Hoskins 1988). To test this, we further decompose Eq. (10) into individual tropical modes as

$$\Delta D_K + \Delta D_R + \Delta D_{HO} \approx \underbrace{\Delta\left(\frac{-v_K^*\,\beta_{\text{eff}}}{f-\partial_y\overline{U}}\right)}_{\text{Sv}_\text{K}} + \underbrace{\Delta\left(\frac{-v_R^*\,\beta_{\text{eff}}}{f-\partial_y\overline{U}}\right)}_{\text{Sv}_\text{R}} + \underbrace{\Delta\left(\frac{-v_{HO}^*\,\beta_{\text{eff}}}{f-\partial_y\overline{U}}\right)}_{\text{Sv}_\text{HO}} \tag{11}$$

where $D = \nabla.\mathbf{v}^*$, Sv denotes Sverdrup effect and the subscripts K, R, HO denote Kelvin, Rossby and higher-order Matsuno modes respectively.

Figure 7 captures the change in divergence/convergence and the change in Sverdrup effect for $U_{\text{jet}} = 34$m/s (Fig. 6d) minus the $U_{\text{jet}} = 0$m/s (Fig. 6a) decomposed into individual tropical modes as in Eq. (11). We find, near the heat source (heat sink) increase in divergence (convergence) is primarily due to amplification of Kelvin-mode (Fig. 7 a-i), while the divergence from Rossby- and higher order Matsuno modes are negligible near the forcing (Fig. 7 a-ii, a-iii). At the same time, the Sverdrup change is dominated by the Rossby-mode and has an amplifying effect on eddy divergence/convergence at the forcing region (notice the same signs in Fig. 7b-ii and Fig. 7a-i).

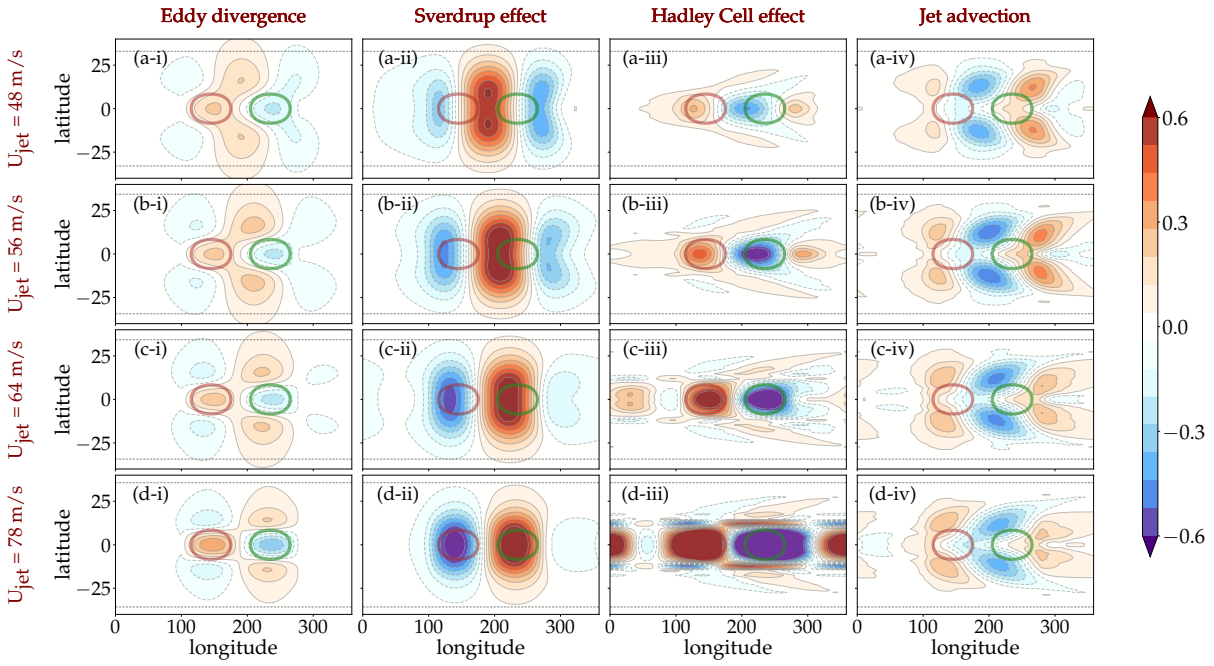

FIG. 8. Same as in Fig. 6 but for the strong jet regime ($U_{jet} > U_c$).

There is little to no Sverdrup effect from the higher-order Matsuno modes and Kelvin-mode (Figs. 7 b-iii, b-i).

The weak-jet regime may be the most relevant for Earth's upper-troposphere since the zonal-mean subtropical jet is rarely found to be any stronger than $\sim 30-35$m/s. This points to an important jet-MJO feedback mechanism in the weak-jet regime which can be summarized as follows. As long as the jet speed is lesser than a critical value ($U_{jet} < U_c$), a stronger jet in response to MJO-like heating leads to stronger subtropical Rossby-mode which by Sverdrup effect amplifies the equatorial Kelvin-mode.

4) STRONG JET REGIME

For jet speeds greater than the critical value ($U_{jet} > U_c$), we see a regime-shift in the role of dynamical processes that feedback onto the local eddy divergence at the forcing region. Figure 8 shows the divergence decomposition for the strong jet cases using Eq. (8). Again, eddy divergence at the forcing region is positive over the heat source and negative over the heat sink (see Fig. 8 a-i to d-i). In contrast to the weak-jet cases, the Hadley cell effect plays the most important role in amplifying the local eddy divergence (see Fig. 8 a-iii to d-iii) while the Sverdrup effect attenuates

it in the strong-jet regime (see Fig. 8 a-ii to d-ii). For all cases zonal wind advection has an almost negligible role on the local divergence, rather its effect is only strong outside of the forcing (see Figs. 6 a-iv to d-iv).

In a strong-jet regime, while the subtropical Rossby-mode is quite pronounced (Figs. 3, A2), the tropical divergence associated with the MJO is dominated by higher-order Matsuno modes rather than the Kelvin-mode. Such regime may be relevant for climate change scenarios or other planetary systems where the subtropical jet and the Hadley cell can become much stronger than that on the Earth. For even stronger jet speeds ($U_{\text{jet}} > 80$ m/s) the model becomes unstable which may indicate another regime transition towards an unstable mode associated with equatorial-superrotation (Showman and Polvani 2011; Potter et al. 2014; Zurita-Gotor and Held 2018) which is beyond the scope of the present study.

To keep the relevance of our results for the Earth's upper-troposphere, here we focus on the weak-jet regime ($U_{\text{jet}} < U_c$), where a stronger jet amplifies both subtropical Rossby-mode and the equatorial-Kelvin mode. Further decomposition of divergence from vorticity budget reveals that the Kelvin divergence and Rossby winds are linked to each other via Sverdrup effect in the presence of a common heat source. This leads to our next question, whether a forced Rossby mode can amplify Kelvin divergence in the absence of heat source?

b. Steady-state response to vorticity forcing and variable jet speed

We now describe the vorticity forcing experiment, involving ensembles of equilibrium runs with variable jet speed, no thermal forcing, and a stationary vorticity forcing in the subtropics resembling the quadrupole Rossby-gyres associated with the MJO. The vorticity forcing is set as the subtropical cyclonic and anticyclonic vortices obtained from one of the steady-states in the thermal forcing experiment where $U_{\text{jet}} = 40$ m/s and is multiplied with a bimodal Gaussian profile along latitude such that the rotational winds peak at 40 degree N/S and are zero at the equator (see Sect. 2.a.2 (ii) and Eq. (5) for details).

Figure 9 shows the steady-state geopotential and wind anomalies in response to the vorticity forcing under different subtropical jet speeds. In the case of no jet, the vorticity forcing induces a strong local response in the subtropics and negligible response in the tropics ($\theta < 15$ N/S) (Fig. 9a). When a jet is present, the same vorticity forcing induces a remote tropical response

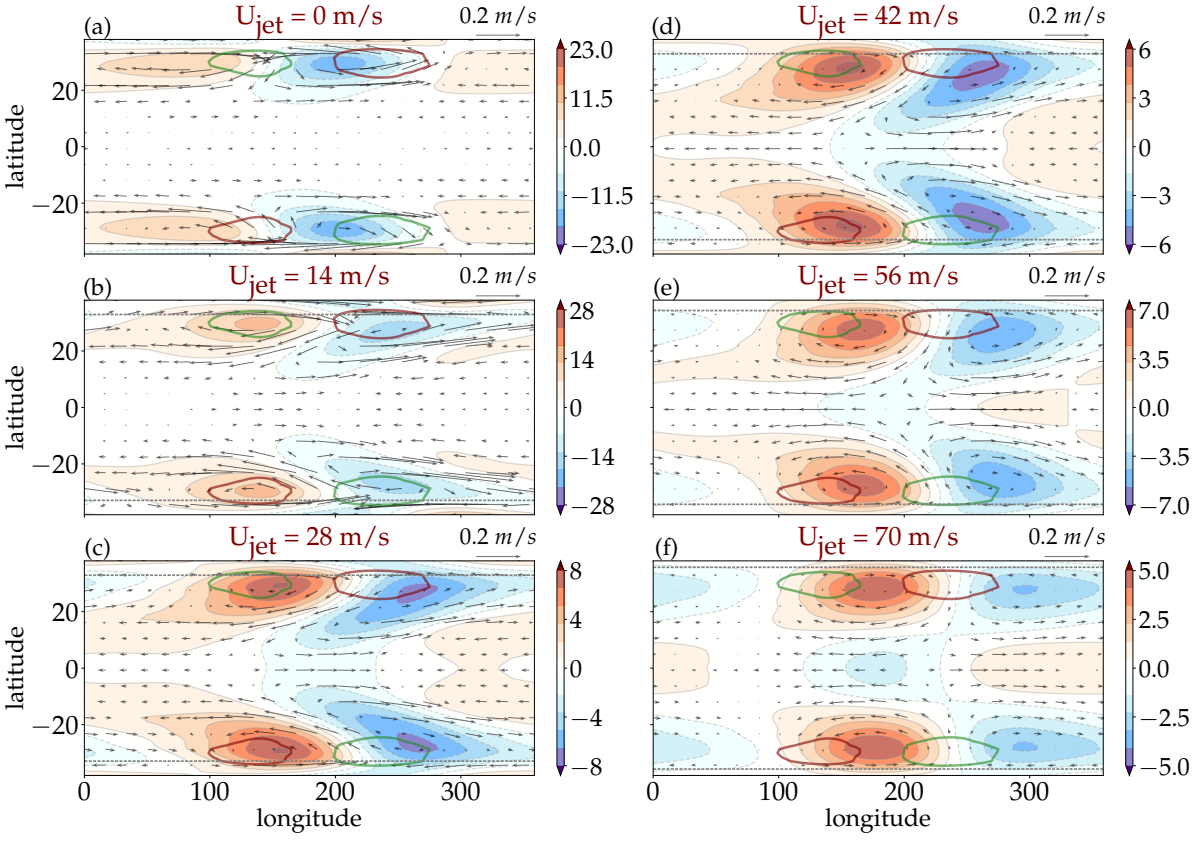

FIG. 9. Same as in Fig. 3 but for the vorticity forcing experiments

that gets stronger with increasing jet speed, as well as a local subtropical response that weakens proportionately, indicating a transfer of energy from the subtropics to the tropics (See Fig. 9 b-f). For U_{jet} = 56 and 70 m/s, the tropical response acquires a well-defined Kelvin structure indicated by the same phase of zonal winds (u^*) and geopotential (ϕ^*) eddies equatorward of 15 N/S (see Figs. 9 e,f). This suggests that even in the absence of equatorial thermal forcing, subtropical Rossby-gyres are able to induce a shear-mediated Kelvin response.

Figure 10 shows the steady-state tropical divergence (measured by D^*_{RMS} between 10N/S latitude) for different values of jet speed in the vorticity forcing experiment (Compare with Fig. 5). When forced with a 'gyre-like' vorticity source in the subtropics, we find that tropical divergence increases with the increase in jet speed up to U_{jet} = 58m/s (see cyan curve in Fig. 10a). This behavior is similar to the divergence-jet speed relationship as seen in the thermal forcing experiment (Compare with Fig. 5) except that the vorticity-induced divergence cannot be explained by the WTG approximation

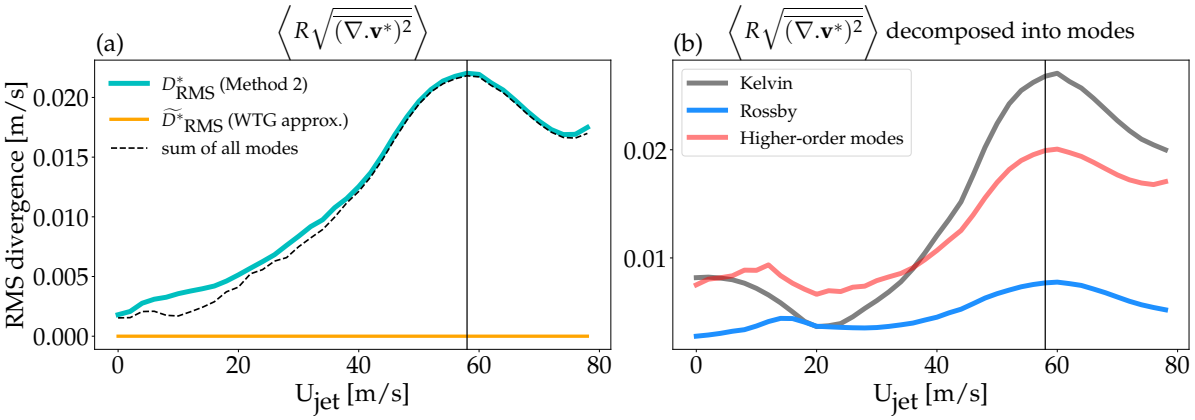

FIG. 10. Same as in Fig. 5 but for the vorticity forcing experiments

($\widetilde{D^*}_{RMS}$). This is because in this case there is no local thermal forcing (F^*_ϕ) at the equator to balance the stretching term in geopotential equation (see yellow dashed curve in Fig. 10a). Furthermore, by decomposing the tropical divergence values into individual Matsuno modes (using the PCF projection method as outlined in Sect. 2b), we find that Kelvin-mode dominates the overall increase in divergence variance (gray curve in Fig. 10b), especially for jet speeds higher than 38 m/s. The contribution by higher-order Matsuno modes is comparatively weaker for stronger jet values (red curve in Fig. 10b), while the tropical Rossby divergence is the weakest (blue curve in Fig. 10b). Interestingly, we also find a critical behavior at a sightly higher jet speed of 58 m/s where the overall tropical divergence (dominated by the Kelvin-mode) decreases with increasing jet speed.

To identify the key dynamical processes behind the jet-speed dependence of the model's divergent response, we look at the divergence - Sverdup effect relationship for the vorticity forcing experiments (see Eq. (10)). Figure 11 shows the change in divergence/convergence and the change in Sverdrup effect for U_{jet} = 56m/s (Fig. 9e) minus the U_{jet} = 0m/s (Fig. 9a) decomposed into individual tropical modes as in Eq. (11). At the equatorial region, we find that an increase in divergence (convergence) is primarily due to an amplification of the Kelvin-mode (Fig. 11 a-i) while the divergence/convergence from Rossby- and higher order Matsuno modes are weaker near the equator (Fig. 11 a-ii, a-iii). At the same time, the Sverdrup change is dominated by the Rossby-mode and has an amplifying effect on eddy divergence/convergence at the equator (see the

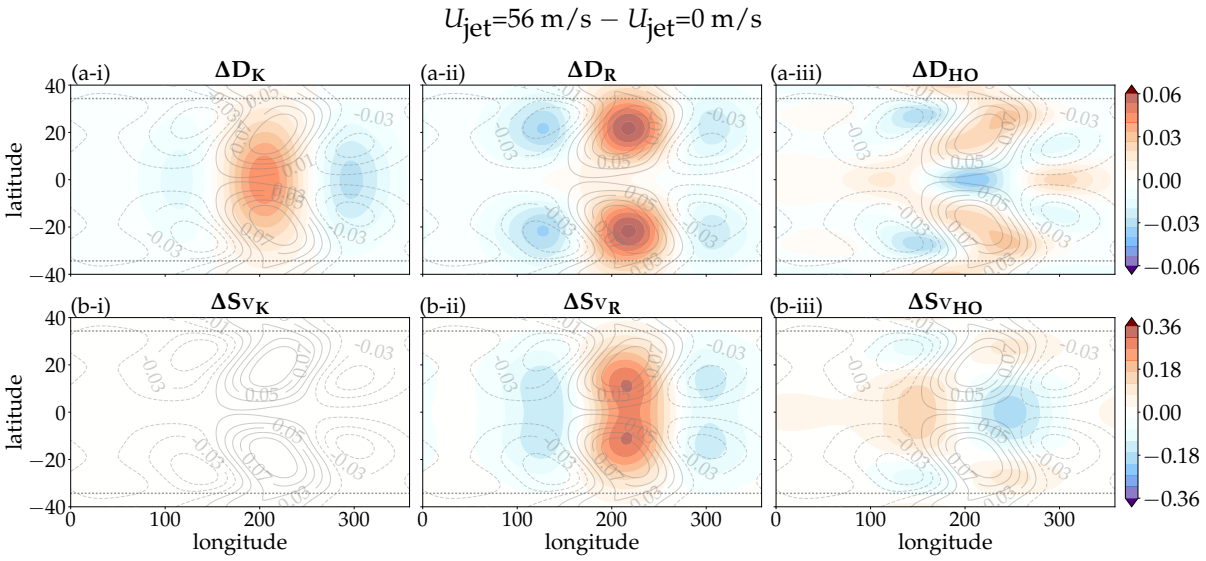

456 FIG. 11. Same as in Fig. 7 but for vorticity forcing experiments showing change in (a) eddy divergence and
457 (b) Sverdrup effect between subtropical jet-state (U_{jet} = 56 m/s) and resting state (U_{jet} = 0 m/s).

467 same signs in Fig. 11b-ii and Fig. 11a-i). There is little to no Sverdrup effect from the higher-order
468 Matsuno modes and Kelvin-mode (Figs. 7 b-iii, b-i).

469 This suggests that in the absence of equatorial thermal forcing, subtropical Rossby-gyres are
470 able to induce a shear-mediated Kelvin response which increases in strength as the jet speed
471 increases up to a critical value. It should be kept in mind that these experiments do not suggest
472 that the Kelvin-mode of the MJO is produced solely by subtropical Rossby-gyres. The point is
473 rather that, in the presence of a zonal-mean meridional wind shear due to the subtropical-jet,
474 the Kelvin and Rossby components of MJO are in close balance with each other via Sverdrup
475 effect. If the jet or the subtropical gyres are strengthened by extrernal processes (for e.g., a low-
476 frequency extratropical wave train from high latitudes, changes in midlatitude temperature gradient
477 or stratospheric forcing), then their effect is felt by the Kelvin-mode circulation potentially leading
478 to enhanced equatorial divergence or convective outflow in the upper-tropospheric circulation of
479 the MJO. In other words, the subtropical Rossby-gyres are coupled to the Kelvin-mode not just by
480 convective heating but also by the zonal-mean meridional wind shear which means the subtropical
481 Rossby gyres act as 'Kelvin wave source' for the tropics, the same way tropical heating acts as
482 'Rossby wave source' in the extratropics (Sardeshmukh and Hoskins 1988).

4. Conclusions and Discussions

a. Potential implications on the vertical structure and amplitude of the MJO

In summary, we found two feedback mechanisms by which the subtropics influences the MJO circulation. The first feedback mechanism is governed by WTG balance and suggests that if the tropical static stability and vertical heating profile responds to changes from the subtropical circulation then the MJO-induced divergence ($\widetilde{D^*}$) should increase with the increase in jet speed across both weak and strong jet regimes. It is not clear yet how effectively this mechanism operates in the real world, since static stability in the tropics is believed to be strongly constrained by moist thermodynamic processes (Stone and Carlson 1979; Betts 1982; Xu and Emanuel 1989). However, some recent studies have shown that such thermodynamic constraints may not be as strict, enabling large-scale circulations to modify free-tropospheric lapse rates (Bao et al. 2022). The cause-and-effect relationship under WTG balance constraints is therefore not clear, and warrants further investigation.

The second feedback mechanism is a deviation from the WTG balance and comes from shear-mediated Rossby-Kelvin coupling due to the 'Sverdup effect'. Under this mechanism, if we assume that the tropical static stability is constant, then MJO divergence (δ_{RMS}) will exhibit a moderate but non-monotonic dependence on the jet speed. Specifically, our results imply that there is a critical jet value at which the Kelvin-mode divergence of the MJO is maximized due to wave-mean flow interaction. The Rossby-Kelvin coupling also plays an important role in meridional moisture advection by the MJO as recently noted by Berrington et al. (2022). Our current climate may be operating in the weak jet regime where the mean subtropical jet is weaker than the critical value, but approaches the critical limit during boreal winter, when the MJO tends to be the strongest.

In reality, both feedback mechanisms may be operating simultaneously and could provide a conceptual framework for understanding: 1) the MJO's response to QBO (Quasi-Biennial Oscillation) phases via changes in subtropical jet speed (Garfinkel and Hartmann 2011a,b; Gray et al. 2018; Martin et al. 2021), 2) the MJO's response to different climate change scenarios (Carlson and Caballero 2016), and 3) the cause of MJO biases in global climate models (Ahn et al. 2020). However, it is important to remember that the conclusions drawn here are based on a highly simplified model with no moisture or cloud radiative processes. For instance, we do not know how much

of the convective outflow generated by the upper-level feedback couples to the low-level MJO convergence/divergence. Depending on the strength of the vertical coupling, it may have different effects on vertical motion, cloud distribution and moisture feedback, which may in turn affect the phase speed of the MJO.

b. Linear versus nonlinear MJO dynamics

It is also worth noting that the results obtained here were derived by running the model in a linear and stable regime. This approach is considered to be realistic, because MJO composites from ERA5 reanalysis dataset reveal that the intraseasonal zonal momentum budget of the MJO during boreal winter is dominated by the linear advection terms (not shown), in accordance with several other observational studies (e.g. Lin et al. (2005); Sakaeda and Roundy (2014)).

However, our approach conflicts with several dry MJO theories that describe the MJO either as a nonlinear phenomenon driven by extratropical forcing (Wedi and Smolarkiewicz 2010; Yano and Tribbia 2017; Rostami and Zeitlin 2020) or a heavily damped Kelvin wave with no role for Rossby waves (Kim and Zhang 2021). TK21 also highlighted the role of nonlinear momentum fluxes on the MJO but they did not evaluate the impact of the linear terms. The effects of nonlinearities might be important for the transient (onset or decay stage) or in moist feedback processes of the MJO. However, the problem of MJO maintenance can be simply explained on the basis of linear dynamics. The linear Rossby-Kelvin feedback mechanism in the lower troposphere may also aid in the eastward propagation of the MJO as noted by Hayashi and Itoh (2017) and may also explain why the MJO tends to be stronger in the Indo-Pacific region, where the subtropical jet is the strongest and closest to the equator during winter-time. A follow-up study will explicitly include the role of zonally varying jet structure on the MJO amplitude in a similar setup.

c. Concluding remarks

Previous studies on MJO dynamics have shown that moisture, cloud radiation and boundary layer processes (Zhang et al. 2020, and references therein) play a crucial role in MJO's initiation and propagation, which we consider as given. Here we focus on the impact of the wintertime subtropical jet in the Indo-Pacific region which sits just north of the MJO dipole and creates substantially strong upper-level horizontal shear for equatorial convective systems. The mean-flow

interaction between MJO convection and the jet gives rise to planetary scale Rossby gyres in the subtropical upper troposphere which forms an integral part of the MJO circulation (Sardeshmukh and Hoskins 1988; Adames and Wallace 2014; Monteiro et al. 2014). The question of whether these forced Rossby gyres and jet structure have any subsequent feedback onto the tropics, is much less understood. Recently Tulich and Kiladis (2021) found considerable weakening of MJO-like signals in idealized SP-WRF calculations when the zonal-mean zonal jet was weakened by 25%, while other parameters like static stability and surface temperature were kept constant.

To understand this result, we used a dry nonlinear shallow water model to examine how the divergent part of its response to an MJO-like thermal forcing is affected by the presence and strength of an imposed subtropical jet. Results showed a positive correlation between equatorial divergence/convergence and subtropical jet speed, but with two different regimes of behavior (weak-jet versus strong-jet). In the weak jet regime, the MJO-induced divergence is amplified due to the 'Sverdrup effect', while in the strong jet regime, the divergence amplifies due to the 'Hadley cell effect'.

To leading order, the divergence induced by the forcing was seen to be well explained by WTG balance ($\widetilde{D^*}$), in accordance with other studies (Sobel et al. 2001; Wolding et al. 2017). In addition, we found an important second-order divergence effect (δ_{RMS}) which peaks at a critical jet speed, U_c and primarily comes from the shear-mediated coupling between subtropical Rossby gyres and the tropical Kelvin mode. This coupling interpretation was further supported by an additional vorticity experiment, which showed how the imposition of subtropical gyre-like forcing induces a Kelvin-mode response near the equator that is strongly dependent on subtropical jet speed. Despite the simplicity of the model set-up, our results point to the potentially important feedback mechanisms by which a subtropical jet can affect the MJO's structure and amplitude.

In summary, we conclude that the MJO cannot be considered as an isolated system in a resting basic state. Even though the convective disturbance may owe its existence to interactions between dry dynamics and moisture, the subtropical jet plays an important role in modifying the upper-tropospheric divergent circulation of the MJO. Future developments of MJO theory should therefore consider the role of the upper-tropospheric background flow even in an idealized system.

Acknowledgments. This research was supported in part by NOAA cooperative agreement NA22OAR4320151 and National Science Foundation (NSF) through award AGS-1839741. P. Barpanda is grateful for the postdoc opportunity supported by NOAA and CIRES.

Data availability statement. The ERA5 reanalysis data can be accessed through the ECMWF website (https://www.ecmwf.int/en/forecasts/datasets/reanalysis-datasets/era5). The shallow water model experiments can be accessed from https://github.com/Pragallva/MJO_waves_meanflow.

References

Adames, and J. M. Wallace, 2014: Three-dimensional structure and evolution of the vertical velocity and divergence fields in the MJO. *Journal of the Atmospheric Sciences*, **71 (12)**, 4661 – 4681, https://doi.org/10.1175/JAS-D-14-0091.1.

Ahn, M.-S., and Coauthors, 2020: MJO propagation across the maritime continent: Are CMIP6 models better than CMIP5 models? *Geophysical Research Letters*, **47 (11)**, e2020GL087 250, https://doi.org/https://doi.org/10.1029/2020GL087250.

Arfken, G. B., and H. J. Weber, 2005: *Mathematical Methods for Physicists*. Elsevier, 1200 pp.

Bao, J., V. Dixit, and S. C. Sherwood, 2022: Zonal temperature gradients in the tropical free troposphere. *Journal of Climate*, 1 – 28, https://doi.org/10.1175/JCLI-D-22-0145.1.

Bao, M., and D. L. Hartmann, 2014: The response to MJO-like forcing in a nonlinear shallow-water model. *Geophysical Research Letters*, **41 (4)**, 1322–1328, https://doi.org/https://doi.org/10.1002/2013GL057683.

Berrington, A. H., N. Sakaeda, J. Dias, and G. N. Kiladis, 2022: Relationships between the eastward propagation of the Madden–Julian Oscillation and its circulation structure. *Journal of Geophysical Research: Atmospheres*, **127 (16)**, e2021JD035 806, https://doi.org/https://doi.org/10.1029/2021JD035806.

Betts, A. K., 1982: Saturation point analysis of moist convective overturning. *Journal of Atmospheric Sciences*, **39 (7)**, 1484 – 1505, https://doi.org/10.1175/1520-0469(1982)039⟨1484:SPAOMC⟩2.0.CO;2.

Carlson, H., and R. Caballero, 2016: Enhanced MJO and transition to superrotation in warm climates. *Journal of Advances in Modeling Earth Systems*, **8 (1)**, 304–318, https://doi.org/ https://doi.org/10.1002/2015MS000615.

Chao, W. C., 1987: On the origin of the tropical intraseasonal oscillation. *Journal of Atmospheric Sciences*, **44 (15)**, 1940 – 1949, https://doi.org/10.1175/1520-0469(1987)044⟨1940:OTOOTT⟩ 2.0.CO;2.

Ferranti, L., T. N. Palmer, F. Molteni, and E. Klinker, 1990: Tropical-extratropical interaction associated with the 30–60 day oscillation and its impact on medium and extended range prediction. *Journal of Atmospheric Sciences*, **47 (18)**, 2177 – 2199, https://doi.org/ 10.1175/1520-0469(1990)047⟨2177:TEIAWT⟩2.0.CO;2.

Frederiksen, J., and C. Frederiksen, 1997: Mechanisms of the formation of intraseasonal oscillations and australian monsoon disturbances: The roles of convection, barotropic and baroclinic instability. *Contributions to Atmospheric Physics*, **70 (1)**, 39–56.

Garfinkel, C. I., and D. L. Hartmann, 2011a: The influence of the quasi-biennial oscillation on the troposphere in winter in a hierarchy of models. part i: Simplified dry gcms. *Journal of the Atmospheric Sciences*, **68 (6)**, 1273 – 1289, https://doi.org/10.1175/2011JAS3665.1.

Garfinkel, C. I., and D. L. Hartmann, 2011b: The influence of the quasi-biennial oscillation on the troposphere in winter in a hierarchy of models. part ii: Perpetual winter waccm runs. *Journal of the Atmospheric Sciences*, **68 (9)**, 2026 – 2041, https://doi.org/10.1175/2011JAS3702.1.

Gehne, M., and R. Kleeman, 2012: Spectral analysis of tropical atmospheric dynamical variables using a linear shallow-water modal decomposition. *Journal of the Atmospheric Sciences*, **69 (7)**, 2300 – 2316, https://doi.org/10.1175/JAS-D-10-05008.1.

Gill, A. E., 1980: Some simple solutions for heat-induced tropical circulation. *Quarterly Journal of the Royal Meteorological Society*, **106 (449)**, 447–462.

Gray, L. J., J. A. Anstey, Y. Kawatani, H. Lu, S. Osprey, and V. Schenzinger, 2018: Surface impacts of the quasi biennial oscillation. *Atmospheric Chemistry and Physics*, **18 (11)**, 8227–8247, https://doi.org/10.5194/acp-18-8227-2018.

Hall, N. M., H. H. Le, and S. Leroux, 2020: The extratropical response to a developing MJO: forecast and climate simulations with the dream model. *Climate Dynamics*, **55 (3)**, 813–829.

Hayashi, M., and H. Itoh, 2017: A new mechanism of the slow eastward propagation of unstable disturbances with convection in the tropics: Implications for the MJO. *Journal of the Atmospheric Sciences*, **74 (11)**, 3749 – 3769, https://doi.org/10.1175/JAS-D-16-0300.1.

Hendon, H. H., and M. L. Salby, 1994: The life cycle of the Madden–Julian Oscillation. *Journal of Atmospheric Sciences*, **51 (15)**, 2225 – 2237, https://doi.org/10.1175/1520-0469(1994)051⟨2225:TLCOTM⟩2.0.CO;2.

Hoskins, B. J., and T. Ambrizzi, 1993: Rossby wave propagation on a realistic longitudinally varying flow. *Journal of Atmospheric Sciences*, **50 (12)**, 1661 – 1671, https://doi.org/10.1175/1520-0469(1993)050⟨1661:RWPOAR⟩2.0.CO;2.

Hsieh, T.-L., C.-Y. Chang, I. M. Held, and P. Zurita-Gotor, 2021: Nonlinear generation of long waves and the reversal of eddy momentum fluxes in a two-layer quasigeostrophic model. *Journal of the Atmospheric Sciences*, **78 (11)**, 3525 – 3536, https://doi.org/10.1175/JAS-D-20-0368.1.

Hsu, H.-H., 1996: Global view of the intraseasonal oscillation during northern winter. *Journal of Climate*, **9 (10)**, 2386 – 2406, https://doi.org/10.1175/1520-0442(1996)009⟨2386:GVOTIO⟩2.0.CO;2.

Jin, F., and B. J. Hoskins, 1995: The direct response to tropical heating in a baroclinic atmosphere. *Journal of Atmospheric Sciences*, **52 (3)**, 307 – 319, https://doi.org/10.1175/1520-0469(1995)052⟨0307:TDRTTH⟩2.0.CO;2.

Kiladis, G. N., K. H. Straub, and P. T. Haertel, 2005: Zonal and vertical structure of the Madden–Julian Oscillation. *Journal of the Atmospheric Sciences*, **62 (8)**, 2790 – 2809, https://doi.org/10.1175/JAS3520.1.

Kiladis, G. N., and K. M. Weickmann, 1992: Circulation anomalies associated with tropical convection during northern winter. *Monthly Weather Review*, **120 (9)**, 1900 – 1923, https://doi.org/10.1175/1520-0493(1992)120⟨1900:CAAWTC⟩2.0.CO;2.

Kiladis, G. N., M. C. Wheeler, P. T. Haertel, K. H. Straub, and P. E. Roundy, 2009: Convectively coupled equatorial waves. *Reviews of Geophysics*, **47 (2)**, https://doi.org/https://doi.org/10.1029/2008RG000266.

Kim, J.-E., and C. Zhang, 2021: Core dynamics of the MJO. *Journal of the Atmospheric Sciences*, **78 (1)**, 229 – 248, https://doi.org/10.1175/JAS-D-20-0193.1.

Knippertz, P., and Coauthors, 2022: The intricacies of identifying equatorial waves. *Quarterly Journal of the Royal Meteorological Society*, **148 (747)**, 2814–2852, https://doi.org/https://doi.org/10.1002/qj.4338.

Knutson, T. R., and K. M. Weickmann, 1987: 30–60 day atmospheric oscillations: Composite life cycles of convection and circulation anomalies. *Monthly Weather Review*, **115 (7)**, 1407 – 1436, https://doi.org/10.1175/1520-0493(1987)115⟨1407:DAOCLC⟩2.0.CO;2.

Kraucunas, I., and D. L. Hartmann, 2007: Tropical stationary waves in a nonlinear shallow-water model with realistic basic states. *Journal of the Atmospheric Sciences*, **64 (7)**, 2540 – 2557, https://doi.org/10.1175/JAS3920.1.

Lau, K.-M., and T. J. Phillips, 1986: Coherent fluctuations of fxtratropical geopotential height and tropical convection in intraseasonal time scales. *Journal of Atmospheric Sciences*, **43 (11)**, 1164 – 1181, https://doi.org/10.1175/1520-0469(1986)043⟨1164:CFOFGH⟩2.0.CO;2.

Lau, N.-C., and K.-M. Lau, 1986: The structure and propagation of intraseasonal oscillations appearing in a gfdl general circulation model. *Journal of Atmospheric Sciences*, **43 (19)**, 2023 – 2047, https://doi.org/10.1175/1520-0469(1986)043⟨2023:TSAPOI⟩2.0.CO;2.

Liebmann, B., and D. L. Hartmann, 1984: An observational study of tropical–midlatitude interaction on intraseasonal time scales during winter. *Journal of Atmospheric Sciences*, **41 (23)**, 3333 – 3350, https://doi.org/10.1175/1520-0469(1984)041⟨3333:AOSOTI⟩2.0.CO;2.

Lin, H., G. Brunet, and J. Derome, 2007: Intraseasonal variability in a dry atmospheric model. *Journal of the Atmospheric Sciences*, **64 (7)**, 2422 – 2441, https://doi.org/10.1175/JAS3955.1.

Lin, H., G. Brunet, and R. Mo, 2010: Impact of the Madden–Julian Oscillation on wintertime precipitation in canada. *Monthly Weather Review*, **138 (10)**, 3822 – 3839, https://doi.org/10.1175/2010MWR3363.1.

675 Lin, J.-L., M. Zhang, and B. Mapes, 2005: Zonal momentum budget of the Madden–Julian
676 Oscillation: The source and strength of equivalent linear damping. *Journal of the Atmospheric*
677 *Sciences*, **62 (7)**, 2172 – 2188, https://doi.org/10.1175/JAS3471.1.

678 Ma, D., and Z. Kuang, 2016: A mechanism-denial study on the Madden–Julian Oscillation with
679 reduced interference from mean state changes. *Geophysical Research Letters*, **43 (6)**, 2989–2997,
680 https://doi.org/https://doi.org/10.1002/2016GL067702.

681 Maloney, E. D., and D. L. Hartmann, 1998: Frictional moisture convergence in a composite life
682 cycle of the Madden–Julian Oscillation. *Journal of Climate*, **11 (9)**, 2387 – 2403, https://doi.org/
683 10.1175/1520-0442(1998)011⟨2387:FMCIAC⟩2.0.CO;2.

684 Martin, Z., C. Orbe, S. Wang, and A. Sobel, 2021: The MJO–qbo relationship in a gcm
685 with stratospheric nudging. *Journal of Climate*, **34 (11)**, 4603 – 4624, https://doi.org/
686 10.1175/JCLI-D-20-0636.1.

687 Matsuno, T., 1966: Quasi-geostrophic motions in the equatorial area. *Journal of the Meteorological*
688 *Society of Japan. Ser. II*, **44 (1)**, 25–43.

689 Matthews, A. J., B. J. Hoskins, and M. Masutani, 2004: The global response to tropical heating in
690 the Madden–Julian Oscillation during the northern winter. *Quarterly Journal of the Royal Me-*
691 *teorological Society*, **130 (601)**, 1991–2011, https://doi.org/https://doi.org/10.1256/qj.02.123.

692 Monteiro, J. M., A. F. Adames, J. M. Wallace, and J. S. Sukhatme, 2014: Interpreting the upper level
693 structure of the Madden–Julian Oscillation. *Geophysical Research Letters*, **41 (24)**, 9158–9165,
694 https://doi.org/10.1002/2014GL062518.

695 Moon, W., G. E. Manucharyan, and H. A. Dijkstra, 2022: Baroclinic instability and large-scale
696 wave propagation in a planetary-scale atmosphere. *Quarterly Journal of the Royal Meteorological*
697 *Society*, **148 (743)**, 809–825, https://doi.org/https://doi.org/10.1002/qj.4232.

698 Potter, S. F., G. K. Vallis, and J. L. Mitchell, 2014: Spontaneous superrotation and the role of
699 kelvin waves in an idealized dry gcm. *Journal of the Atmospheric Sciences*, **71 (2)**, 596 – 614,
700 https://doi.org/10.1175/JAS-D-13-0150.1.

Ray, P., and T. Li, 2013: Relative roles of circumnavigating waves and extratropics on the MJO and its relationship with the mean state. *Journal of the Atmospheric Sciences*, **70 (3)**, 876 – 893, https://doi.org/10.1175/JAS-D-12-0153.1.

Ray, P., and C. Zhang, 2010: A case study of the mechanics of extratropical influence on the initiation of the Madden–Julian Oscillation. *Journal of the Atmospheric Sciences*, **67 (2)**, 515 – 528, https://doi.org/10.1175/2009JAS3059.1.

Rostami, M., and V. Zeitlin, 2019: Eastward-moving convection-enhanced modons in shallow water in the equatorial tangent plane. *Physics of Fluids*, **31 (2)**, 021 701, https://doi.org/10.1063/1.5080415.

Rostami, M., and V. Zeitlin, 2020: Can geostrophic adjustment of baroclinic disturbances in the tropical atmosphere explain MJO events? *Quarterly Journal of the Royal Meteorological Society*, **146 (733)**, 3998–4013, https://doi.org/https://doi.org/10.1002/qj.3884.

Rui, H., and B. Wang, 1990: Development characteristics and dynamic structure of tropical intraseasonal convection anomalies. *Journal of Atmospheric Sciences*, **47 (3)**, 357 – 379, https://doi.org/10.1175/1520-0469(1990)047⟨0357:DCADSO⟩2.0.CO;2.

Sakaeda, N., and P. E. Roundy, 2014: The role of interactions between multiscale circulations on the observed zonally averaged zonal wind variability associated with the Madden–Julian Oscillation. *Journal of the Atmospheric Sciences*, **71 (10)**, 3816 – 3836, https://doi.org/10.1175/JAS-D-13-0304.1.

Sardeshmukh, P. D., and B. J. Hoskins, 1988: The generation of global rotational flow by steady idealized tropical divergence. *Journal of Atmospheric Sciences*, **45 (7)**, 1228 – 1251, https://doi.org/10.1175/1520-0469(1988)045⟨1228:TGOGRF⟩2.0.CO;2.

Schwendike, J., G. J. Berry, K. Fodor, and M. J. Reeder, 2021: On the relationship between the Madden–Julian Oscillation and the hadley and walker circulations. *Journal of Geophysical Research: Atmospheres*, **126 (4)**, e2019JD032 117, https://doi.org/https://doi.org/10.1029/2019JD032117.

Seo, K.-H., and H.-J. Lee, 2017: Mechanisms for a pna-like teleconnection pattern in response to the MJO. *Journal of the Atmospheric Sciences*, **74 (6)**, 1767 – 1781, https://doi.org/10.1175/JAS-D-16-0343.1.

Showman, A. P., and L. M. Polvani, 2011: Equatorial superrotation on tidally locked exoplanets. *The Astrophysical Journal*, **738 (1)**, 71, https://doi.org/10.1088/0004-637X/738/1/71, URL https://dx.doi.org/10.1088/0004-637X/738/1/71.

Sobel, A. H., J. Nilsson, and L. M. Polvani, 2001: The weak temperature gradient approximation and balanced tropical moisture waves. *Journal of the Atmospheric Sciences*, **58 (23)**, 3650 – 3665, https://doi.org/10.1175/1520-0469(2001)058⟨3650:TWTGAA⟩2.0.CO;2.

Stone, P. H., and J. H. Carlson, 1979: Atmospheric lapse rate regimes and their parameterization. *Journal of Atmospheric Sciences*, **36 (3)**, 415 – 423, https://doi.org/10.1175/1520-0469(1979)036⟨0415:ALRRAT⟩2.0.CO;2.

Straus, D. M., and R. S. Lindzen, 2000: Planetary-scale baroclinic instability and the MJO. *Journal of the Atmospheric Sciences*, **57 (21)**, 3609 – 3626, https://doi.org/10.1175/1520-0469(2000)057⟨3609:PSBIAT⟩2.0.CO;2.

Tseng, K.-C., E. Maloney, and E. Barnes, 2019: The consistency of MJO teleconnection patterns: An explanation using linear rossby wave theory. *Journal of Climate*, **32 (2)**, 531 – 548, https://doi.org/10.1175/JCLI-D-18-0211.1.

Tulich, S. N., and G. N. Kiladis, 2021: On the regionality of moist kelvin waves and the MJO: The critical role of the background zonal flow. *Journal of Advances in Modeling Earth Systems*, **13 (9)**, e2021MS002 528, https://doi.org/https://doi.org/10.1029/2021MS002528, e2021MS002528 2021MS002528.

Wang, B., and H. Rui, 1990: Dynamics of the coupled moist kelvin–rossby wave on an equatorial β-plane. *Journal of Atmospheric Sciences*, **47 (4)**, 397 – 413, https://doi.org/10.1175/1520-0469(1990)047⟨0397:DOTCMK⟩2.0.CO;2.

Wedi, N. P., and P. K. Smolarkiewicz, 2010: A nonlinear perspective on the dynamics of the MJO: Idealized large-eddy simulations. *Journal of the Atmospheric Sciences*, **67 (4)**, 1202 – 1217, https://doi.org/10.1175/2009JAS3160.1.

Weickmann, K. M., G. R. Lussky, and J. E. Kutzbach, 1985: Intraseasonal (30–60 day) fluctuations of outgoing longwave radiation and 250 mb streamfunction during northern winter. *Monthly*

Weather Review, **113 (6)**, 941 – 961, https://doi.org/10.1175/1520-0493(1985)113⟨0941:IDFOOL⟩2.0.CO;2.

Wolding, B. O., E. D. Maloney, S. Henderson, and M. Branson, 2017: Climate change and the Madden–Julian Oscillation: A vertically resolved weak temperature gradient analysis. *Journal of Advances in Modeling Earth Systems*, **9 (1)**, 307–331, https://doi.org/https://doi.org/10.1002/2016MS000843.

Xu, K.-M., and K. A. Emanuel, 1989: Is the tropical atmosphere conditionally unstable? *Monthly Weather Review*, **117 (7)**, 1471 – 1479, https://doi.org/10.1175/1520-0493(1989)117⟨1471:ITTACU⟩2.0.CO;2.

Yang, G.-Y., B. Hoskins, and J. Slingo, 2003: Convectively coupled equatorial waves: A new methodology for identifying wave structures in observational data. *Journal of the Atmospheric Sciences*, **60 (14)**, 1637 – 1654, https://doi.org/10.1175/1520-0469(2003)060⟨1637:CCEWAN⟩2.0.CO;2.

Yano, J.-I., and J. J. Tribbia, 2017: Tropical atmospheric Madden–Julian Oscillation: A strongly nonlinear free solitary rossby wave? *Journal of the Atmospheric Sciences*, **74 (10)**, 3473 – 3489, https://doi.org/10.1175/JAS-D-16-0319.1.

Zhang, C., A. F. Adames, B. Khouider, B. Wang, and D. Yang, 2020: Four theories of the Madden–Julian Oscillation. *Reviews of Geophysics*, **58 (3)**, e2019RG000 685, https://doi.org/https://doi.org/10.1029/2019RG000685.

Zhang, C., and P. J. Webster, 1992: Laterally forced equatorial perturbations in a linear model. part i: Stationary transient forcing. *Journal of Atmospheric Sciences*, **49 (7)**, 585 – 607, https://doi.org/10.1175/1520-0469(1992)049⟨0585:LFEPIA⟩2.0.CO;2.

Zurita-Gotor, P., and I. M. Held, 2018: The finite-amplitude evolution of mixed kelvin–rossby wave instability and equatorial superrotation in a shallow-water model and an idealized gcm. *Journal of the Atmospheric Sciences*, **75 (7)**, 2299 – 2316, https://doi.org/10.1175/JAS-D-17-0386.1.

APPENDIX A

Meridional mode decomposition

The dry equatorial waves, i.e. Kelvin, Rossby, mixed Rossby-Gravity (MRG) and Inertia-Gravity (IG) modes, were originally derived by Matsuno (1966) as orthonormal eigen modes of an unforced linear shallow water system on an equatorial β plane with a resting basic state. Later Gill (1980) extended this problem and showed that the steady-state solution to a forced shallow water system is a linear superposition of Rossby, Kelvin and MRG modes (IG modes decay to zero in a damped steady-state). The Matsuno-Gill modes (hereafter Matsuno modes) have a characteristic meridional structure, given by the Parabolic cylinder function (PCF) of degree m, which is expressed as

$$D_m\left(\frac{\theta}{\theta_T}\right) = 2^{-m/2} exp\left(-\frac{1}{2}\left(\frac{\theta}{\theta_T}\right)^2\right) H_m\left(\frac{\theta}{\theta_T}\right) \tag{A1}$$

where various parameters in Eq. (A1) are defined as follows: $H_m\left(\frac{\theta}{\theta_T}\right)$ is the Physicist's Hermite polynomial of degree $m \geq 0$, θ is latitude in radians, $\theta_T = (1/R)\sqrt{c/\beta_o}$ is the equatorial trapping scale in radians, $\beta_o = 2\Omega/R$ where Ω, R are the angular velocity and radius of the Earth respectively. Replacing β with $\beta - \partial^2_{yy}\overline{U}$ did not change the modal decomposition results, so we used the same trapping scale, θ_T for all U_{jet} experiments.

Our shallow water system is neither on a β plane nor does it have a resting basic state (spherical model with a background horizontal shear). However the final steady-state solutions can be approximated as linear superposition of Matsuno modes up to meridional truncation number N. This is the same as Galerkin method of discretization and has been successfully used in reanalysis dataset for identifying equatorial waves (Yang et al. 2003; Gehne and Kleeman 2012; Knippertz et al. 2022). We take the same approach for decomposing our steady-state shallow water model response into Matsuno modes as described below.

We define new variables, q, r, ν from the model output where $q = u^* + \phi^*/c$, $r = u^* - \phi^*/c$ and $\nu = v^*$. $c = \sqrt{g h_{\text{eq}}}$ is the average gravity wave speed of the shallow-water model where h_{eq}=500m

The variables, q, r, v can be expressed as the weighted sum of the orthogonal PCF modes, i.e.

$$q(\lambda,\theta) = q_0(\lambda) D_0\left(\theta/\theta_T\right) + q_1(\lambda) D_1\left(\theta/\theta_T\right) + \sum_{n\geq 1}^{N} q_{n+1}(\lambda) D_{n+1}\left(\theta/\theta_T\right) \tag{A2}$$

$$v(\lambda,\theta) = \sum_{n\geq 1}^{N} v_n(\lambda) D_n\left(\theta/\theta_T\right) \tag{A3}$$

$$r(\lambda,\theta) = \sum_{n\geq 1}^{N} r_{n-1}(\lambda) D_{n-1}\left(\theta/\theta_T\right) \tag{A4}$$

where n is an integer and $N = 10$ is the meridional truncation number and Matsuno mode coefficients are given by (q_{n+1}, v_n, r_{n-1}). Using Matsuno (1966)'s convention, $n = -1$ corresponds to the Kelvin-mode whose coefficients are $(q_0, 0, 0)$; $n = 0$ corresponds to the MRG mode whose coefficients are $(q_1, 0, 0)$, $n = 1$ corresponds to the lowest order Rossby-mode whose coefficients are (q_2, v_1, r_0) and $n \geq 2$ correspond to other higher-order Matsuno modes whose coefficients are (q_{n+1}, v_n, r_{n-1}). Note that the odd-integer mode coefficients are not present in our shallow water model since the background-mean state and the forcings are all symmetric about the equator. Thus, the contribution of antisymmetric Matsuno modes like the MRG, and the antisymmetric Rossby and IG modes, are negligible in our experiments.

Each of the coefficients in Eqs. (A2-A4) is determined by projecting the nth-order PCF on to q, r, v respectively and using the orthogonality relation for PCF functions. For example, $v_n(\lambda) = \frac{1}{\sqrt{\pi} n! \theta_T} \int_{-\pi/2}^{+\pi/2} v(\lambda,\theta)\, D_n\left(\theta/\theta_T\right) d\theta$ for $n \geq 0$. The same projection formula applies to other coefficients, q_n and r_n.

Once all the mode coefficients (q_{n+1}, v_n, r_{n-1}) are determined, the eigenvector for each mode in terms of winds and geopotential can be expressed as

$$\text{Kelvin: } \begin{pmatrix} u_K \\ v_K \\ \phi_K \end{pmatrix} = \frac{1}{2} \begin{pmatrix} q_0 D_0 \\ 0 \\ c\,(q_0 D_0) \end{pmatrix} \tag{A5}$$

$$\text{Rossby: } \begin{pmatrix} u_R \\ v_R \\ \phi_R \end{pmatrix} = \frac{1}{2} \begin{pmatrix} q_2 D_2 + r_0 D_0 \\ v_1 D_1 \\ c\,(q_2 D_2 - r_0 D_0) \end{pmatrix} \tag{A6}$$

$$\text{Higher order: } \begin{pmatrix} u_{HO} \\ v_{HO} \\ \phi_{HO} \end{pmatrix} = \frac{1}{2} \begin{pmatrix} \sum_{n>2}^{N} (q_{n+1} D_{n+1} + r_{n-1} D_{n-1}) \\ \sum_{n>2}^{N} (v_n D_n) \\ \sum_{n>2}^{N} c\,(q_{n+1} D_{n+1} - r_{n-1} D_{n-1}) \end{pmatrix} \tag{A7}$$

It is important to note here that Eqs. (A5-A7) represent forced Matsuno modes in the steady-state or at a timescale much slower than the the gravity wave speed (c) of the shallow-water model. This is equivalent to looking at the equatorial waves when the normalized frequency is close to 0, i.e. $\frac{\omega}{\sqrt{c\beta_o}} \to 0$. Thus $n = 1$ mode (Eq. (A6)) corresponds to a pure Rossby wave and does not include any contribution from the IG modes unlike the case of a transient Matsuno mode when $\frac{\omega}{\sqrt{c\beta_o}} \gg 0$.

For the same set of steady-state experiment documented in Figure 3 and 4, here we show the decomposition of steady-state response into individual Matsuno modes as outlined in Sect. 2.b.1.

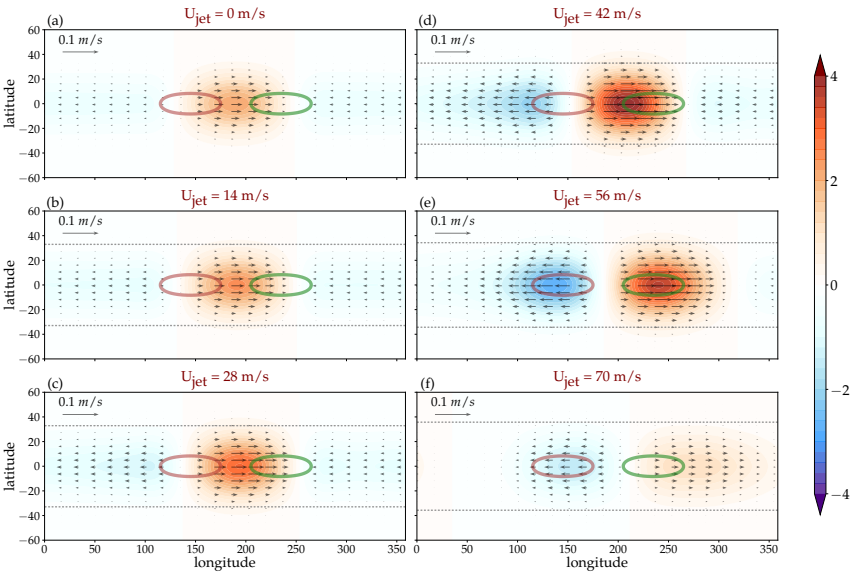

827 FIG. A1. Same as in Fig. 3 but for Kelvin-mode component of the circulation showing eddy geopotential, ϕ_K^*
828 in colors $[m^2/s^2]$ and wind vectors, $\mathbf{v}_K^*$ [m/s] as defined in eqs 6 and A5

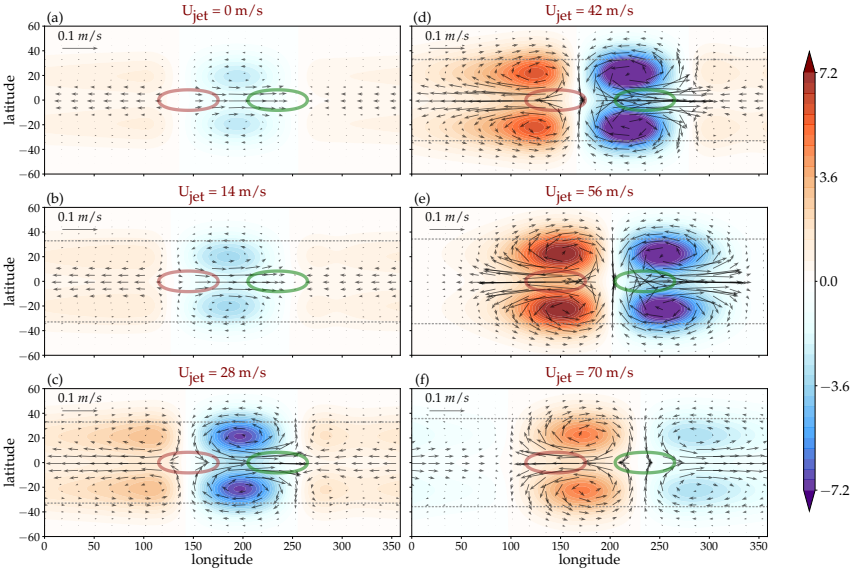

829 FIG. A2. Same as in Fig. 3 but for Rossby-mode component of the circulation showing eddy geopotential, ϕ_R^*
830 in colors [m^2/s^2] and wind vectors, $\mathbf{v}_R^*$ [m/s] as defined in eqs 6 and A6

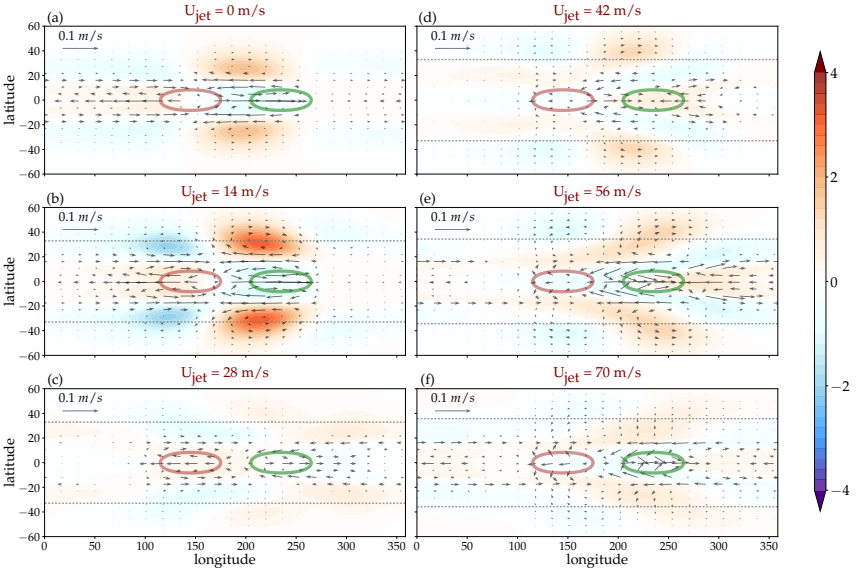

FIG. A3. Same as in Fig. 3 but for higher-order Matsuno modes showing eddy geopotential, ϕ^*_{HO} in colors [m^2/s^2] and wind vectors, $\mathbf{v}^*_{HO}$ [m/s] as defined in eqs 6 and A7

APPENDIX B

Steady-state model response using Method 1

Here we show that the Method 1 is comparable to Method 2. See Sect. 2a for description of both methods.

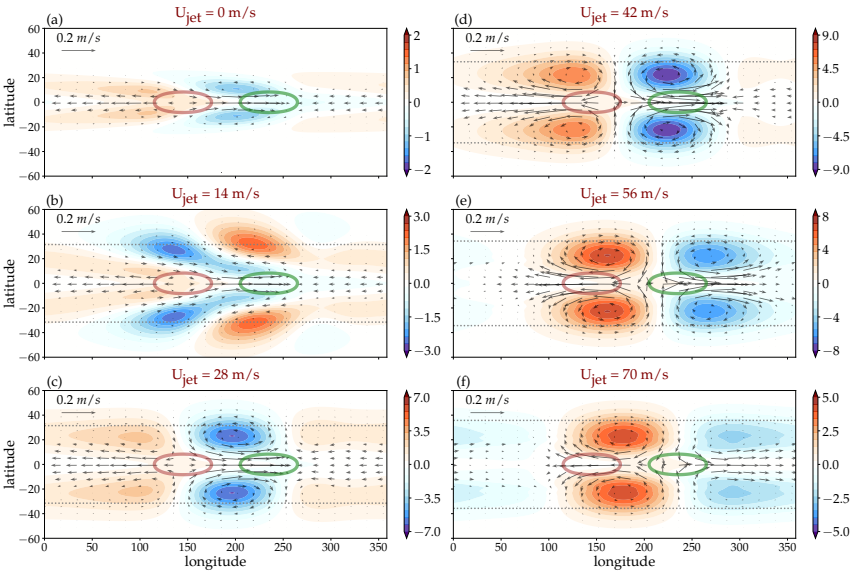

FIG. B1. Steady-state response to fixed thermal forcing and changing jet speeds. Same as in Fig. 3 but using Method 1

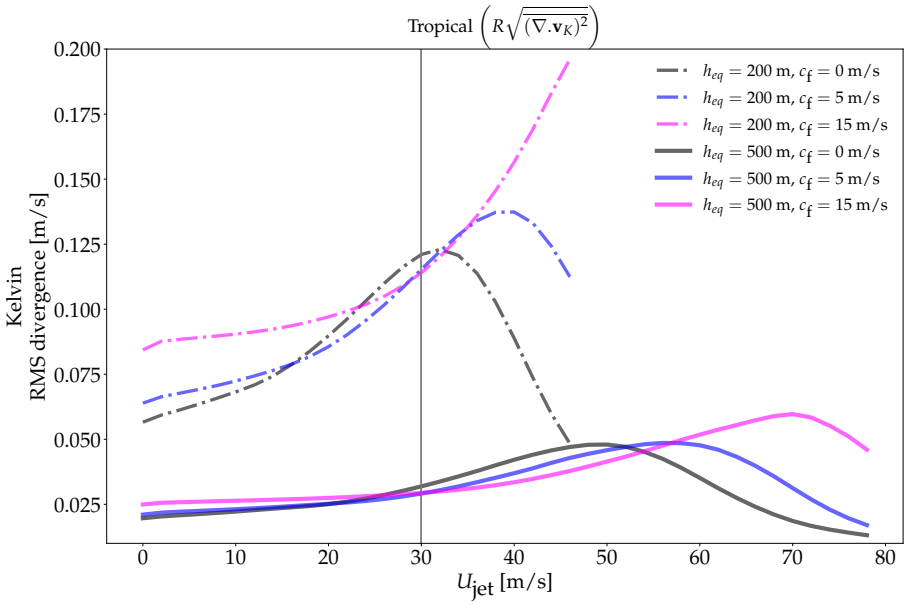

FIG. C1. RMS Kelvin divergence in the tropics in response to thermal forcing with different phase speeds (c_f), different jet speeds (U_{jet}) and different equivalent depths (h_{eq}). The RMS divergence is averaged over 10S−10N and is rescaled by the radius of Earth, R. The black vertical line indicates Earth's zonal-mean jet speed in the Northern Hemisphere during winter

APPENDIX C

Sensitivity of Kelvin divergence to changing equivalent depth and forcing phase speeds

In the main results, we have shown the effect of jet strength on a steady-state forcing with h_{eq} =500 m. Here we explore the sensitivity of our experiments to changing equivalent depths, which is a measure of effective static stability in the atmosphere and non-stationary thermal forcing which represents the effect of convectively coupled Kelvin waves moving at different phase speeds.

Figure C1 captures results from several thermal forcing experiments showing root-mean-square of Kelvin divergence (averaged between 10S to 10N) for a wide range of jet speeds for two equivalent depths (h_{eq} = 200m and 500m) and 3 different forcing phase speeds (c_f = 0 m/s, 5 m/s and 15 m/s) but with a fixed heating amplitude. Note that the critical jet speed (U_c) is not a constant, rather it is lowered for smaller gravity-wave speed ($c = \sqrt{gh_{eq}}$) and smaller forcing phase speed (c_f), i.e. U_c is small when c and c_f are small.